Cement and Concrete Composites 108 (2020) 103514

Contents lists available at ScienceDirect

Cement and Concrete Composites

journal homepage: http://www.elsevier.com/locate/cemconcomp

Engineering of high specific strength and low thermal conductivity cementitious composites with hollow glass microspheres for high-temperature high-pressure applications

Konrad J. Krakowiak [a,*], Raj Gopal Nannapaneni [a], Amir Moshiri [a], Tejasree Phatak [a], Damian Stefaniuk [b], Lukasz Sadowski [b], Mohammad Javad Abdolhosseini Qomi [c]

[a] Civil and Environmental Engineering Department, Cullen College of Engineering, University of Houston, Engineering Building 1, Room N-132, 4726 Calhoun Road, Houston, TX, 77204-4003, USA

[b] Faculty of Civil Engineering, Wroc aw University of Science and Technology, Wybrzeże Wyspiańskiego 27, 50-370, Wroc aw, Poland

[c] Department of Civil and Environmental Engineering, Henry Samueli School of Engineering, E4130 Engineering Gateway, University of California, Irvine, Irvine, CA, 92697-2175, USA

ARTICLE INFO

Keywords:
Lightweight concrete
Oil-well cement
Hydrothermal curing
Microstructure
Hollow microspheres
Thermal properties

ABSTRACT

Lightweight cement-based composites with high specific strength and low thermal conductivity are highly sought in the energy and construction industries. These characteristics are important in designing cement liners for high-temperature, high-pressure (HTHP) wells, in addition to those operating in permafrost. Similar attributes are also desirable in designing cementitious composites for energy efficient building envelopes. This work reports the results of an experimental campaign focused on engineering lightweight cementitious composites with hollow glass microspheres. It is demonstrated that the chemical stability of microspheres at HTHP conditions can be directly controlled by modulating the specific surface area and dissolution rate constant of supplementary siliceous additives. In addition to the stabilizing effect, such additives lead to the pore structure refinement and the enhancement of interfacial transition zone (ITZ). Introduced lightweight composites are capable of delivering significant load bearing capacity when normally cured, which is greatly increased by hydrothermal curing. Such high specific strength composites possess thermal conductivity below 0.3 W/mK at the oven dry density <1000 kg/m^3 and cement dosage <400 kg/m^3. This class of cementitious composites bears potential to enhance zonal insulation and well integrity, as well as increasing energy efficiency of building envelopes.

1. Introduction

The enhanced thermal insulation combined with the adequate mechanical performance are desired parameters of cement liner in high-temperature, high-pressure (HTHP) wells, as well as oil and gas wells operating in permafrost in polar regions e.g. North Slope, Alaska [1]. In both cases the difference between the temperature of produced fluid and the temperature of the host formation, can generate significant thermal stresses in the cement casing system. If not accounted for, the overall local stress resulting from the superposition of the thermal load and fluid pressure, which can reach up to around 140 MPa in HTHP wells [2], can cause cracking and severely compromise the well integrity. Moreover, in the absence of adequate thermal insulation of the casing, the permafrost thawing takes place leading to such effects as ground subsidence, buckling and cracking of the casing, ultimately compromising well integrity [1,3].

On the other spectra of relevant applications of Portland cement is the structural concrete. It can deliver long-term performance, while ensuring cost-effectiveness at the same time. These attributes make concrete a leading material in surface infrastructure projects. However, concrete is relatively poor thermal insulator, which sets back the application of this material in building envelopes. For example, for the average wall thickness of 15 cm (6) in residential buildings across North America, normal to medium density concrete can only provide thermal resistance (R-value) around 0.18 Km^2/W (1 h F ft^2/BTU) (Fig. 1a). Therefore, the construction of energy efficient building envelopes requires concrete to be used in conjunction with insulating materials e.g. glass bats, polymer foams or cellular glass boards, which have

* Corresponding author.
E-mail address: kjkrak@uh.edu (K.J. Krakowiak).

https://doi.org/10.1016/j.cemconcomp.2020.103514
Received 31 May 2019; Received in revised form 25 November 2019; Accepted 7 January 2020
Available online 10 January 2020
0958-9465/Published by Elsevier Ltd.

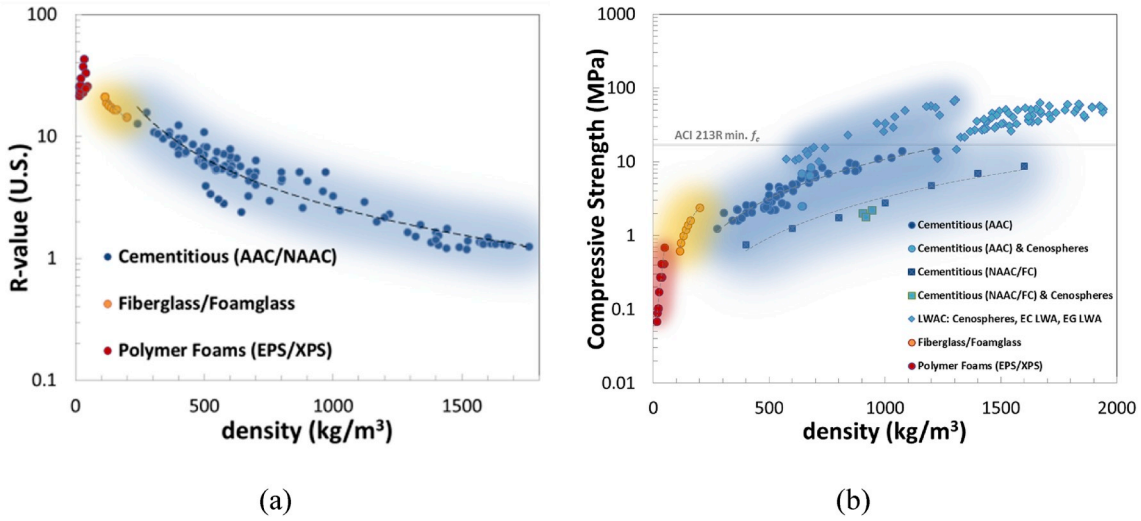

Fig. 1. Available literature data on the relation between: (a) thermal resistance vs. dry bulk density (b) compressive strength vs. density. R-values (U.S.), in hr F ft^2/BTU are calculated for 6 (15.24 cm) barrier thickness, SI R-Value 0.176 R-Value (U.S.) conversion applies. AAC/NAAC: autoclaved/non-autoclaved (foamed) aerated concrete, EPS/XPS: expanded/extruded polystyrene, EC/EG: expanded clay, glass light weight aggregate. Data compiled from Refs. [4 21].

minimal or none structural properties, e.g. strength.

1.1. Key material factors

The first key factor affecting thermal performance of cement paste is the intrinsic heat conductivity of calcium-silicate-hydrate (C-S-H) and portlandite (CH), two dominant microstructural phases in hydrated cement systems [22,23]. Recent study analyzing vibrational densities of states (VDOS) in C-S-H molecular structure estimates the volumetric effective thermal conductivity of C-S-H equal to k_v 0.98 0.2 W/mK [24]. Thermal conductivity of CH is even higher with its estimated volume average k_v 1.32 0.2 W/mK [24]. Therefore, to offset the low insulating potential of microstructural phases, including conventional aggregates, it is a common practice in oil and gas industry to reduce concrete density by introducing air (k 0.026 W/mK) voids in the amount beyond the porosity value inherently associated with w/c ratio [22,25]. However, the density reduction severely degrades mechanical performance of concrete (Fig. 1b), thus compromises its specific strength.

The second pertinent issue affecting thermal resistance of cement liner, is the vulnerability of this class of materials to moisture uptake by the open system of capillary and gel pores. The increase in the moisture content of hydrated cement paste effectively decreases paste s overall thermal resistance caused by the high thermal conductivity of water (0.6 W/mK) [24].

1.2. Lightweight concrete: mechanical performance, density and thermal resistance

According to American Concrete Institute (ACI) lightweight concrete is classified based on its 28 day air dry unit weight as: (a) structural concrete with the density ranging from 1350 to 1900 kg/m^3 displaying the minimum compressive strength of 17 MPa, (b) moderate strength concrete with the density between 800 and 1350 kg/m^3 and intermediate compressive strength 7 < fc < 17 MPa, and (c) low density concrete with the density in the range 300 800 kg/m^3 used primarily for non-loadbearing elements as an insulation [26].

Lightweight structural concrete uses lightweight aggregate as complete or partial replacement of the conventional aggregates. Typical aggregates include expanded slag, shale and clay, as well as slag, pumice, scoria and recently cenospheres, in conjunction with supplementary cementitious materials as partial cement replacement [25,26]. Although ACI places minimum strength requirement of 17 MPa, in practice, strength values up to around 50 MPa are common [7,9,27 30] and show clear positive correlation with the bulk dry density (Fig. 1b). Depending on the mix design and processing technology, cement content may vary from 300 to 600 kg/m^3. On average, lightweight structural concrete displays thermal conductivity in the range from 0.4 to around 1 W/mK in the oven dry state, which increases with increasing moisture content [11,26,31 33].

By lowering its overall bulk density, a moderate strength concrete displays a further decrease in the thermal conductivity. k-values in the range from 0.2 to 0.4 W/mK are commonly reported [5,11,26]. However, as expected, higher concentration of air voids, which is usually achieved by greater incorporation of lightweight aggregate or introduction of the air-entraining agent (foam agent), further reduces its load bearing capacity. In the lack of any significant molecular scale modification to the properties of OPC-based cementitious matrix, dominated by C-S-H and CH [22,25], as well as lightweight aggregate, the strength loss can be easily explained by gel/space ratio reduction, as originally observed by Powers and Brownyard for Portland cement mortars [25]. With the packing efficiency of C-S-H gel relatively constant and contained within two morphologies: a) low-density (LD-C-S-H) 64% packing efficiency, and b) high-density (HD-C-S-H) 74% packing efficiency [34,35], the reduction in gel/space ratio reflects the increasing free volume of cement system occupied by capillary and air-voids (air--entrained and/or entrapped pores).

Finding the balance between thermal and mechanical properties of the low-density concrete (density below 800 kg/m^3) has been the subject of extensive investigation in the recent years. This refers to the effect of mix composition [5,13,15,36,37], processing [5,14], as well as mix design strategies [13,38]. A special attention has been placed on the alternatives to conventional light-weight aggregates such as cenospheres [8,10,14,39], cellular glass LWA [13], and recently aerogel powder [40 42]. Listed aggregates offer several advantages: a closed pore structure with very low water absorption reduces the water ingress thus making the cement-composite less vulnerable to moisture changes, due to their low density they effectively contribute to lowering thermal conductivity of the cement composite, and their glass shell can provide extra reinforcement to the air voids helping in sustaining the local stresses exerted on the pore walls. For typical values of thermal conductivity in the range 0.1 < k < 0.2 W/mK, this technological modification lead to substantial enhancement of specific strength as compared to conventionally produced normal and autoclaved aerated concrete (AAC). Still, to the best of authors knowledge, their load-bearing capacity is below minimum required for structural applications [25,26].

Table 1
Design and processing parameters of investigated cement systems.

	System	
	T1 (lightweight)	T2 (neat)
$_{sl}$ (kg/m^3)	1204	1890
SVF (%)*	68	41
cement (kg/m^3)**	356	1300
silica (kg/m^3)**	242	
-spheres (kg/m^3) **	285	
w/c (w/s)	0.89 (0.36)	0.45
SP (mL/kg cem.)	987	
(Ca/Si)$_{mix}$	0.75	
pre-curing	25 C for 7/14/28 days	25 C for 7/14/28 days
HTHP curing	24 h at 175 C, hydrothermal <5 MPa	none

* SVF solids volume fraction, ** - per 1 m^3 of paste.

In this work, the authors present an original experimental development focused on addressing existing limitations in thermal and mechanical performance of cement-based composites for applications in oil-well cement systems in particular. This is achieved by incorporating hollow glass microspheres and micro-silica in the cement-paste microstructure subjected to the normal and elevated temperature curing conditions. Engineered cement composites are studied with respect to microstructure development, thermo-mechanical performance as well as -spheres stability. This includes analysis of pore network with N_2 gas adsorption and mercury porosimetry, phase composition with X-ray diffraction and electron microscopy, as well as thermal and mechanical properties measured in standardized tests.

2. Materials and methods

2.1. Materials synthesis

For this study a set of samples were prepared using Class G oil-well cement (Lafarge-Holcim): lightweight cement formulation at the water-to-solid ratio 0.36, and auxiliary neat cement system at water-to-cement ratio 0.45 (Table 1). Crystalline silica MIN-U-SIL®5 (US-Silica), with the median particle size d_{50} 2 m was used in the lightweight composite T1. 3 M hollow soda-lime-borosilicate glass -spheres with the median particle size d_{50} 16 m, apparent density 0.6 g/cm^3, average wall thickness 0.70 m, and isostatic crush strength of 186 MPa (90% survival rate [43]) were used as a lightweight filler. The workability and consistency of the pastes were adjusted with the high-range water reducing admixture (MasterGlenium 7700, BASF). After homogenization in the high-shear mixer (RZR 21002, Heidolph), pastes were casted into PC cylindrical molds (h 22 70 mm) and cured under saturated conditions for 7, 14 and 28 days prior to hydrothermal curing at 175 C. Similar curing at room temperature was employed in neat cement paste, however, the hydration process was arrested at specific time intervals via the solvent exchange method.

Hydrothermal curing was run in the 500 ml stainless steel chemical reactor (Col-INT Tech) with controlled curing schedule: initial pressure 9 bar (helium), 90 min linear temperature increase from room temperature to 175 C, 24hr hold period followed by natural cooling.

2.2. X-ray powder diffraction

Representative samples for x-ray powder diffraction were extracted at the mid-height of each specimen. Circular discs covering the entire cross-section of the original specimen, and approximately 1 mm thick, were submerged in isopropyl alcohol for 2 h followed by manual wet grinding in alcohol using an agate mortar [44]. Powdered samples were dried and stored under vacuum until testing. All powder diffraction patterns were collected with a PANalytical X Pert PRO XRPD multipurpose diffractometer configured in Bragg-Brentano geometry, with a high-speed, high-resolution X Celerator position sensitive detector, and a Cu anode source (Cu K-alpha 1.541 Å). Scans were carried out from 5 to 60 /2 , with a step size of 0.009 and a speed of 0.5 s/step. Experimental x-ray patterns were analyzed in HighScore Plus® (PANalytical) package and compared to Powder Diffraction Files (PDF) from the database published by the International Centre for Diffraction Data (ICDD).

2.3. Mercury intrusion porosimetry

Mercury intrusion porosimetry (MIP), AutoPore IV 9500 instrument (Micromeritics, US), was used to assess the medium and large capillary porosity, as well as the pore size distribution. The intrusion pressure ranged from 3.5 10 ^{3} MPa 455 MPa, discretized into 70 pressure steps equally spaced on a logarithmic scale, equilibration time 15 s, evacuation pressure 50 m Hg, and mercury filling pressure 3.5 10 ^{3} MPa. A value of 140 was assumed for the contact angle, and 0.48 N/m for the surface tension of mercury [45]. Thin disks of cement paste were oven dried to a constant weight at 105 C. Two samples per specimen were analyzed (with mass of around 0.6 g), given an excellent reproducibility of the MIP measurements. The bulk density was determined at an intrusion pressure level of 13.8 10 ^{3} MPa. The pore size classification proposed by Mindess et al. [25], and previously used in the description of the pore domain evolution of conventional oil well cement systems [46,47], is applied in this work.

To complete the characterization of the pore domain, the total evaporable water content was determined by oven drying of a saturated surface dry paste to a constant weight at 105 C. Sample was considered to achieve constant weight when the difference in weight between two consecutive recordings dropped below 0.5% over the period of 24 h. On average, six samples (cylindrical disks 22 mm in dimeter and 5 mm thick) per batch were tested before and after exposure to hydrothermal conditions.

2.4. N_2 gas adsorption (BET)

Nitrogen gas adsorption was used to gain insight into the effect of accelerated curing on the relative changes of fine pore structure, which could not be completely recapitulated by mercury intrusion technique. Indeed, the MIP pore inference is constrained by the high intrusion pressure required to infiltrate fine voids, which can cause damage to the pore structure [48,49], but more important by the isostatic crush strength of hollow glass -spheres, 193 MPa [43]. Intrusion beyond this pressure limit is required to access fine pores. For this experiment, specimens were analyzed in the automated multiport gas sorption instrument Micromeritics 3Flex (Norcross, USA). Disks of saturated paste were degassed to a constant weight at 105 C, crushed into small particles, and coarse ground with mortar and pestle. On average, three samples of each paste were tested, and the sample weight was kept around 1 g. The post-processing of the experimental output was executed with the MicroActive (Micromeritics) data analysis software. The pore distribution was determined according to BJH method by analyzing the desorption branch of the isotherm [50 52].

2.4.1. Comment on selected method of sample preparation

It is well established that direct drying has significant drawbacks on preservation of cement paste microstructure [22,25,53,54]. The stresses related to the surface tension of receding menisci can lead to shrinkage and alter the pore structure. Comparing to other less detrimental preparation strategies e.g. D-drying, solvent exchange, the systematic coarsening is reported in PSD obtained on 105 C dried pastes. However, this downside comes with a benefit of significantly reducing the total time of water removal. This is especially evident in hydrothermally cured specimens, which have much finer pore structure [46] (Fig. 2). Therefore, conventional drying was consistently applied across all

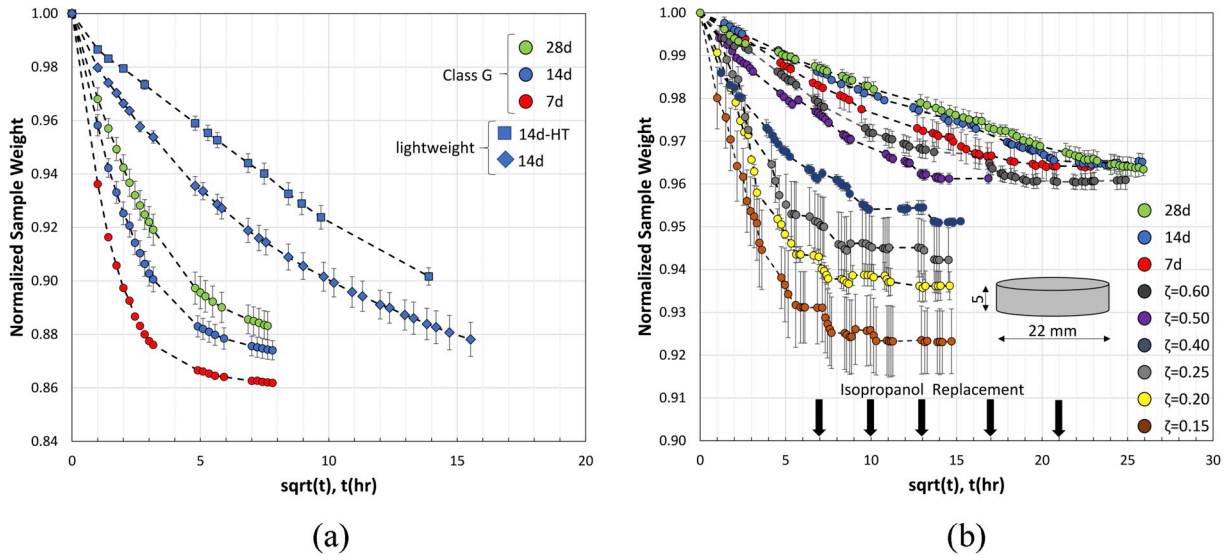

Fig. 2. Effect of microstructure densification on the kinetics of water removal in conventional drying at 50 C (a), and in water removal by solvent exchange with isopropanol (b).

samples given the project timeframe, instruments availability, as well as selected sample geometry. Consequently, MIP and N_2 adsorption measurements carried out in this study are used for the purpose of general inference of the impact of accelerated curing on the relative changes of void structure domain between the samples, rather than to perform quantitative analysis of the undisturbed pore system in hardened paste.

To cross-validate the observed trends in pore structure changes across investigated specimens, an auxiliary Class G cement paste was synthesized (Table 1). The hydration of this paste was arrested at particular time intervals corresponding to different values of hydration degree, including 7, 14 and 28 days (Fig. 2). At each age, thin circular disks of paste were extracted and dried by solvent exchange method using isopropanol. The solvent to sample volume ratio was set at 50:1, the isopropanol was frequently replaced, and the samples were left immersed until stabilization of their weights. This stage was followed by the conventional degassing at 50 C prior to MIP and N_2 testing.

2.5. Scanning electron microscopy

Secondary electron micrographs were acquired at 15eV accelerating voltage, 35 spot size and 11 mm working distance (JEOL 6010LA). Prior to imaging, small fragments extracted from the central part of the specimen tested in compression were dried, and the surface was coated with the conductive layer of carbon to prevent charge build-up. Secondary electron (SE) images were acquired at magnification range from X150 to X3000 and image resolution 5120 3840 pixels.

2.6. X-ray micro-computed tomography (CT)

X-ray microtomography (CT) was employed to gain insight into the effect of hydrothermal curing on the microstructure of lightweight cement system. In particular, the chemical stability of hollow glass -spheres was investigated. Cement paste samples were dry cut with low speed diamond saw into rectangular prisms 3 3 5 mm, which were further reduced in size to 1.5 1.5 4 mm by gentle grinding on a 320 grit SiC paper. Final step included sample cleaning with dry compressed air.

In order to expose the hollow glass -spheres in which the integrity of the shell was compromised, either by mechanical action or chemical interactions, previously dried and vacuum degassed T1 sample was immersed for 24hrs in 3% iodine solution. Due to its high x-ray absorption, iodine solution is commonly used as a contrast enhancing agent in the CT tomography [55,56]. Samples were scanned using SkyScan 1172 (Bruker microCT, Kontich, Belgium) and each scan took approximately 12 h. Detailed CT analytical conditions are listed in Table 2.

Table 2
Scanning parameters for the samples before and after immersion in an iodine solution.

Scanning parameter	Before immersion	After immersion
Pixel size [m/px]	0.74	0.74
Voltage [kV]	59	89
Current (A)	167	112
Exposure Time [ms]	2650	2650
Filter	Al, 0.5 mm	Al, 0.5 mm
Angle rotation step [ ]	0.18 up to 360	0.18 up to 360

3D microstructure reconstruction was carried out on 2D projections following Feldkamp algorithm [57] (Fig. 3). Median and Kuwahara filters [58,59] were applied to all CT scans. Finally, the volume-of-interest (VOI) selected for consecutive statistical analysis was reduced to 1.0 1.0 0.5 mm inner prism. VOI size reduction was directed to minimize the bias in the statistical analysis caused by the boundary effects e.g. microstructure damage due to grinding. Statistical analysis of the reconstructed microstructure was performed with the help of Wolfram Mathematica computing package. Prior to quantitative analysis the image segmentation was performed based on the deconvolution of the gray level histogram. Moreover, a manual size threshold of 40 m was prescribed in order to separate macroscopic air voids from the hollow glass microspheres. This size corresponds to the iM30K particle top diameter [43].

2.7. Thermal conductivity

Disk-like cement paste specimens, 22 mm in diameter and 6 mm in thickness, were dried at 105 C to constant weight. Next, top and bottom surfaces were polished with P1200, P2500 and P4000 SiC sand papers (CarbiMet, Buehler) to minimize surface roughness and ensure good contact with the instrument plates. In the final stage, top and bottom surfaces were cleaned with pressurized dry air and stored in the desiccator prior to testing. Thermal conductivity was measured with heat flow meter FOX 50 (TA Instruments, 10 mm diameter transducer) according to ASTM standards C518 04 and E 1530 06 [60,61]. For all

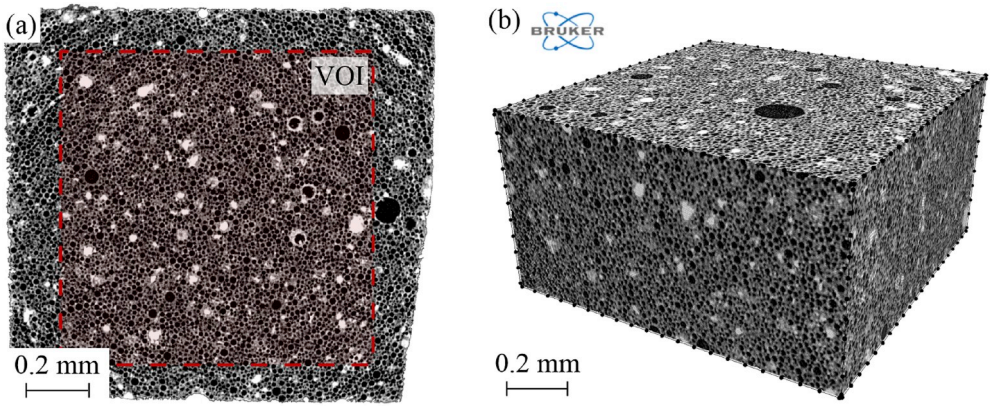

Fig. 3. Reconstructed microstructure of the lightweight T2 cement system (room temperature curing for 28 days) obtained with computed x-ray microtomography: (a) 2D projection after image processing, (b) 3D reconstruction.

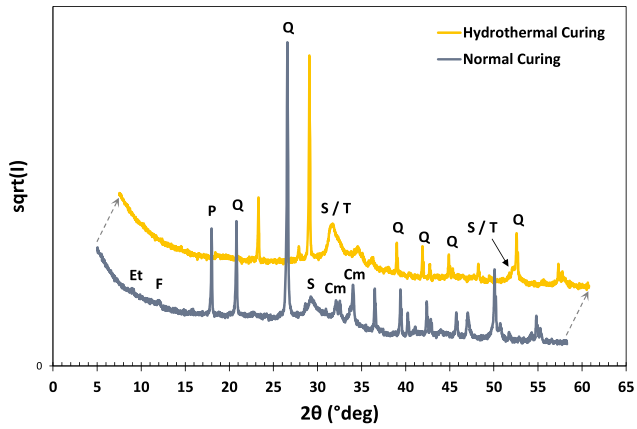

Fig. 4. X-ray powder diffraction spectra of investigated lightweight cement system (T1) cured in normal (20 C) and hydrothermal conditions (175 C). Et ettringite, Cm unreacted cement clinker, P portlandite, Q low quartz, S C-S-H, T tobermorite. Hydrothermal curing spectra shifted at 2 axis for clearer presentation.

specimens, the upper plate temperature was set to 25 C and the lower plate to 15 C. Two-thickness method was used to account for the thermal contact resistance [62].

2.8. Compressive strength

Synthesized samples were tested for unconfined compressive strength according to ASTM standard procedure [63]. Cylindrical specimens, 22 mm in diameter and 44 mm in height, were tested after curing in the saturated conditions for 7, 14, 28 days, as well as after HTHP treatment. Top and bottom surfaces of the cylinders were grinded with the sand paper to achieve smooth finish and to minimize possible tilt. On average, six specimens were evaluated for each batch in the universal testing machine (Instron 5969, Illinois) at the stress rate of 0.25 0.05 MPa, which was determined on the trial specimen measured prior to the batch testing.

3. Experimental results

3.1. X-ray diffraction and qualitative phase analysis

X-ray powder diffraction results of normally cured and hydrothermally cured specimens are presented on Fig. 4. As expected, in the normally cured cement system the crystalline phases of cement hydration include: portlandite (CH) with its strongest lines at 2 {18.01,34.1} and ettringite (AFt) with its characteristic lines at {9.09,15.78}. However, the latter shows very weak reflections above the background, which can be the result of low cement content in the investigated mix as well as low abundance of C_3A and gypsum in Class G cement [64]. Moreover, a characteristic diffraction hump may be observed in the range 2 {25; 35}, which is typical feature of semi-amorphous calcium-silicate-hydrate (C-S-H) gel [22,47]. Other crystalline phases present in this sample are -quartz with major peaks at 2 {20.85, 26.63} and unreacted clinker.

Hydrothermal processing significantly alters the mineralogical composition of the matrix. The portlandite peaks are no longer present in the spectra and the intensities of -quartz lines are substantially reduced. This observation is a direct evidence of thermally activated pozzolanic reaction in which both phases take an active part and the pozzolanic C-S-H gel and/or nanocrystalline tobermorite product is formed [22,46,47,65 67]. The formation of pozzolanic calcium silicate hydrates is reflected by the increased intensity of diffuse reflections centered at around 29.4 , 31.9 and 49.5 . The observed spectra shows strong similarities to XRD patterns recorded on the hydrothermally cured high density silica-enriched cement systems discussed in detail in previous work [46].

3.2. Bulk dry density, porosity and pore structure

Bulk dry density and open porosity results are presented in Table 3 for investigated samples. Overall, cement system, T1, displays very comparable values of dry bulk density in the range 915 940 kg/m^3, which are not significantly affected by the type of applied curing conditions and duration of curing. However, hydrothermal curing tends to slightly increase open porosity. Such increase is especially evident in 7 days old samples, for which the absolute difference in measured porosity is significantly larger than recorded standard deviation.

Cumulative mercury intrusion curves are displayed on Fig. 5. In the room temperature cured pastes the first breakthrough point on the intrusion curve is recorded in the domain of capillary pores (>50 nm [25]). However, the characteristic pore size corresponding to this breakthrough point systematically shifts toward smaller value as the sample age increases. Such behavior is typical for hydrating cement systems in which products of cement hydration build up in the inter-particle space previously occupied by the pore solution. This effect is demonstrated with the help of auxiliary data, obtained on neat Class G cement paste (T2 system), in which the intrusion curves were recorded at different values of degree of hydration (see Fig. 5c). The densification of the inter-particle space with the advancement in the cement hydration is evident and in complete analogy to changes taking place in the lightweight T1 system cured from 7 to 28 days.

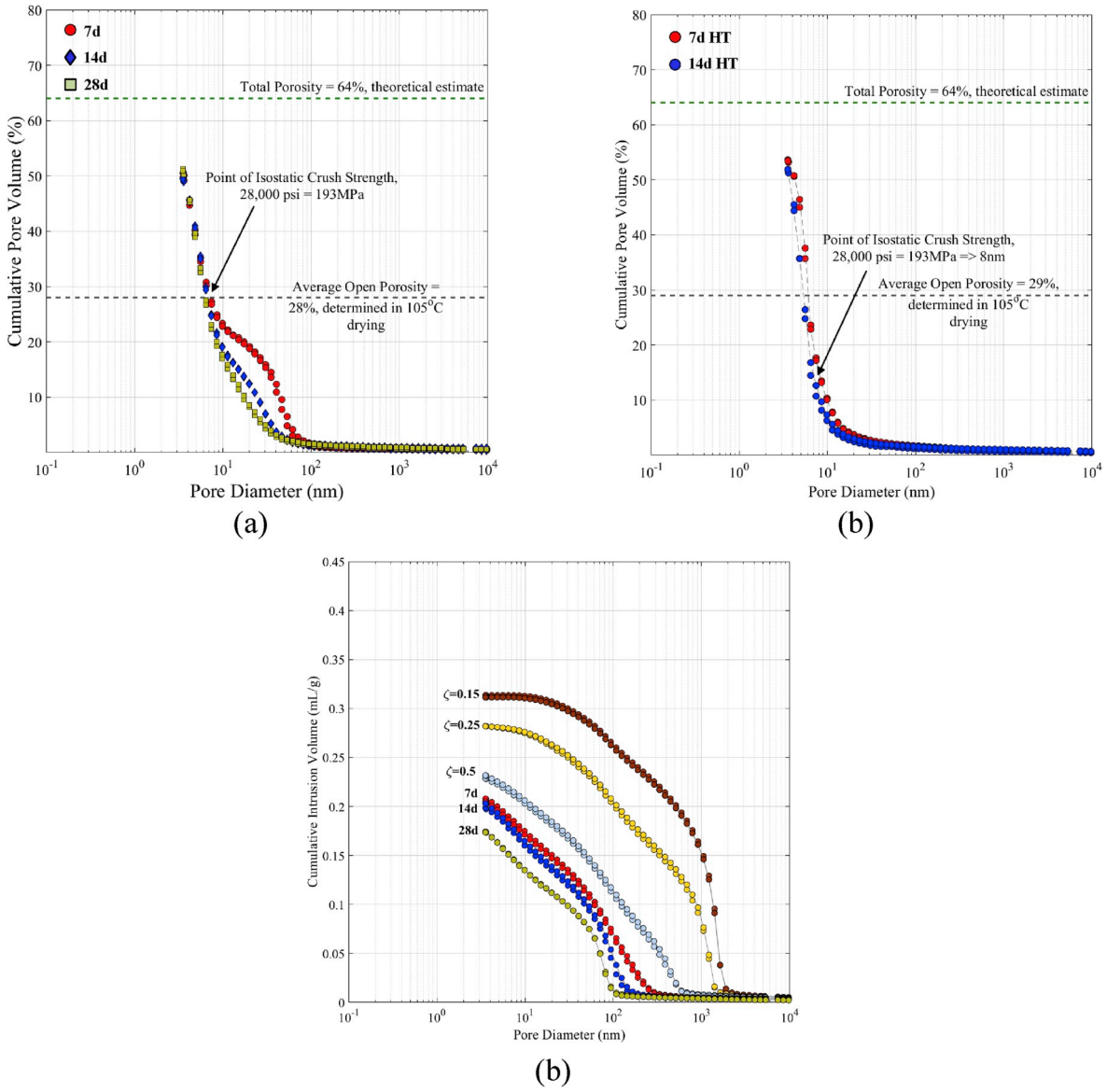

Fig. 5. Mercury intrusion curves obtained on: (a) lightweight T1 cement system cured at room temperature from 7 to 28 days, (b) and after hydrothermal curing at 175 C, (c) auxiliary Class G cement paste at w/c 0.45 cured up to 28 days (corresponds to degree of hydration).

It must be remembered, the working principle of the MIP technique is the intrusion of the *open porosity* domain with the non-wetting fluid. Accordingly, the use of the Washburn equation [68] allows to relate the pressure to the physical characteristic size of the void and infer the pore size distribution (in the sense of the pore throat size [45]) in the solid. Given this principle, any intrusion in the normally cured paste recorded beyond the open porosity threshold, which was determined from the total evaporable water content (see Table 3 and Fig. 5), must correspond to mercury invading the closed porosity. This can only happen upon previous collapse of the hollow glass -spheres due to excessive stresses exerted on theirs walls. In fact, the manufacture s data for iM30K glass bubbles specify the isostatic crush strength at 193 MPa (28,000 psi) [43], which would correspond to the intrusion pressure through 8 nm "fictitious pore throat. As displayed on Fig. 6, the second breakthrough in the MIP curves closely aligns with this limiting pressure, and most of the intrusion beyond this threshold does not correspond to probing a physical pore structure of even finer morphology. Finally, the maximum recorded cumulative pore volume reaches the value 50%, which is still below 64%, the theoretical estimate of the total porosity in both systems. In fact the max. pressure (414 MPa) in the measurements corresponds to pore diameter 3.6 nm, therefore, MIP was not able to probe any open pore below this threshold size. Additionally, the existence of some residual fraction of glass microspheres which eventually might have survived the intrusion cycle cannot be excluded.

Hydrothermal processing of investigated lightweight system T1 leaves a significant impact on the pore structure and the intrusion behavior, respectively (see Fig. 5b). First, no significant intrusion takes place in the pore size corresponding to the large and medium capillary voids. Second, the breakthrough intrusion point is located at around 10 nm pore throat dimeter, and in very close proximity to the point of the isostatic strength of the glass bubbles. The observed differences, in particular the lack of capillary pore domain, points toward fine pore structure dominated by the gel pores and characterized by much lower hydraulic permeability.

3.3. N_2-gas adsorption and fine pore structure

Results of the N_2 physisorption recorded on normal and

hydrothermally cured lightweight cement pastes are presented on Fig. 6. In both cases, IUPAC Type IVa adsorption isotherms with H3 hysteresis are observed. These types of isotherms are commonly given by mesoporous solids [51,52]. Recorded isotherms do not display plateau associated with the limiting uptake at high P/P_0, instead they rise rapidly indicating the presence of capillary pores (macropores according to IUPAC classification) [52]. The Type H3 loop is also characteristic of mesoporous materials in which loosely coherent plate-like particles assemble into an aggregate giving rise to slit-shaped pores. This observation is coherent with the current view on C-S-H gel meso-structure, in which layered structure particles, assembled into globules, cluster together in two different packing densities, high-density HD C-S-H and low density LD C-S-H, respectively [34,35,69]. However, a significant difference, between normal and hydrothermal cured pastes, is observed in the lower portion of isotherms corresponding to N_2 uptake in micropores (see Fig. 6a). Much higher adsorption in the latter case points toward more refined pore structure with greater contribution of gel pores comparing to the former. More insight into this result is gained with the help of standard BET-plots (see Fig. 6b), which show a linear relation between $P/(Q\ (P\text{-}P_0))$ and P/P_0 in the range 0.05 0.25. Although the estimate of parameter C is comparable between the specimens, C values in the approximate range 80 150 are indicative of monolayer-multilayer adsorption process [51,52], the monolayer capacity (n_m) in the hydrothermally cured paste is almost double that of normally cured. Therefore, higher specific surface area (SSA) may be expected in this case. In fact, the SSA values estimated from BET-plots (Fig. 6b) read 26 m^2/g for HT-cured paste and 16 m^2/g for normal paste, respectively. However, given the controversy surrounding the use of N_2 to assess the SSA of cement-based materials [54], as well as applied degas protocol, these quantitative estimates must be taken with caution and be used only for qualitative comparison.

Fig. 6c and d depict trends in the Barrett-Joyner-Halenda [50] pore size distribution inferred from the desorption branch of the isotherm. Regardless of the duration of pre-curing in the standard conditions, the hydrothermal treatment results in finer pore structure dominated by gel pores. This result suggests that hydrothermal processing of low maturity lightweight pastes, e.g. 7 days, tends to lead to similar end-point in the microstructure transformation as cement pastes pre-cured for longer times. Described observations are is in line with the MIP results reported earlier in the text.

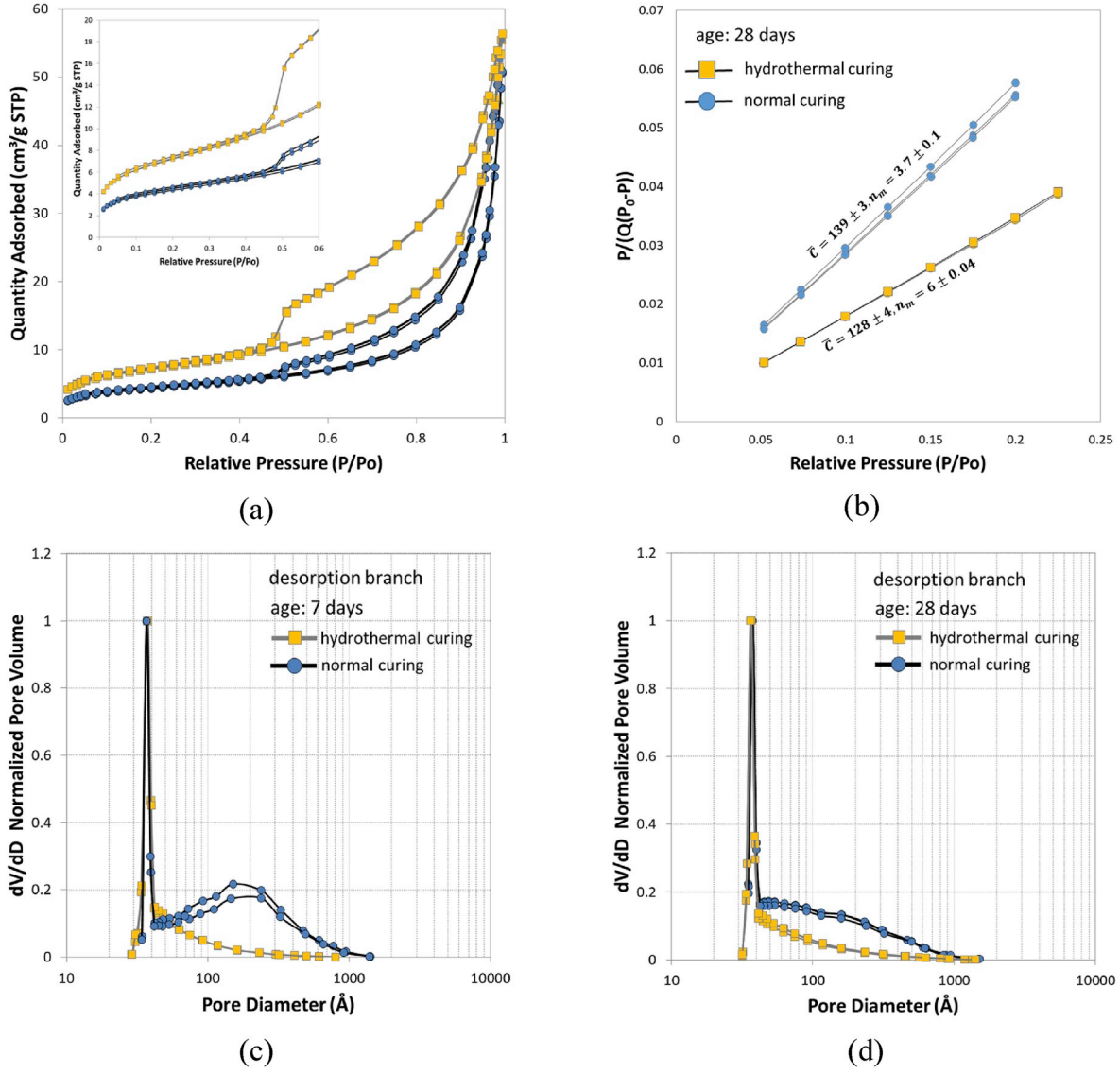

Fig. 6. N_2 adsorption-desorption isotherms (a) and corresponding BET-plots (b) for 28 days old pastes cured in saturated conditions at 20 C (blue) and followed by hydrothermal curing at 175 C (yellow), (c d) BJH pore size distribution derived from desorption branch for 7 days and 28 days old pastes. (For interpretation of the references to colour in this figure legend, the reader is referred to the Web version of this article.)

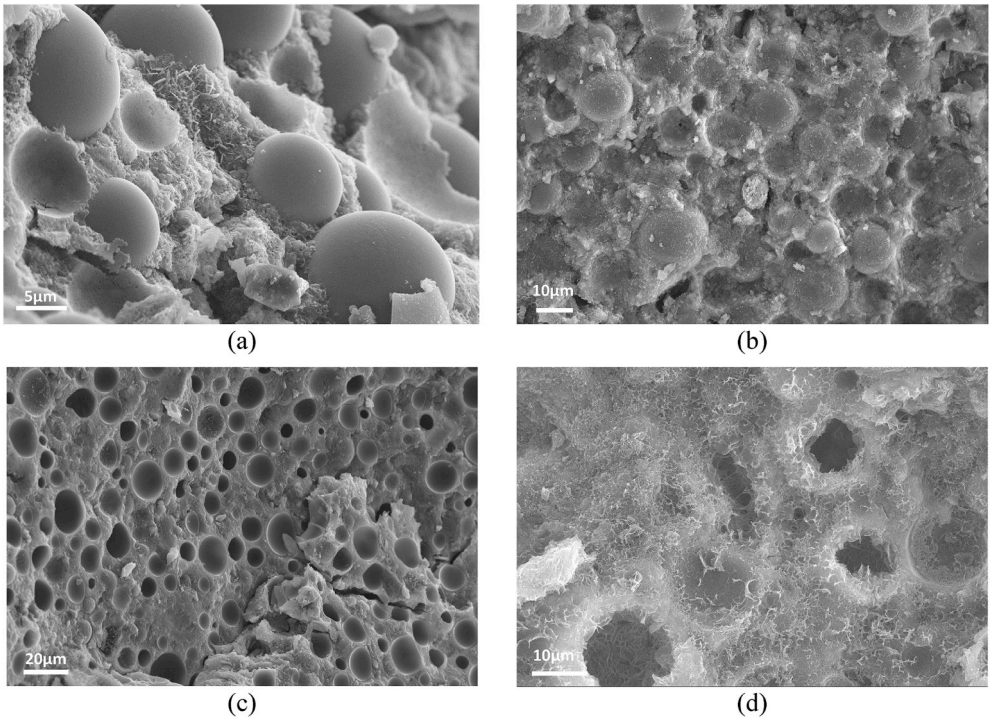

Fig. 7. Secondary electron micrographs of T2 (Class G) system: (a) after 7 days standard curing at 20 C, (b) 14 days standard curing, (c,d) 7 days standard curing followed by hydrothermal curing at 175 C for 24hr.

3.4. Microstructure

3.4.1. Scanning electron microscopy

Secondary electron micrographs of T1 fractured surfaces, before and after exposure to hydrothermal processing, are presented on Fig. 7. Hollow glass microspheres tend to be distributed uniformly across matrix dominated by the cement hydration products intermixed with silica. No tendency toward the clustering of spheres was observed. At the submicron scale, the observed smooth profile of the microspheres after fracture suggests very limited physicochemical interaction of the borosilicate glass with the cement hydration products at the curing age of 7 days (Fig. 7a). The fracture pattern also points toward relatively weak interfacial bond between spheres and the matrix (Figs. 7a and 8a). On the other hand, the texture of the microspheres in the sample aged for 14 and 28 days display higher roughness, more frequent surface defects, and residual matrix material remaining on the surface after the fracture (Fig. 7b).

In contrary to standard saturated curing, hydrothermal processing at 175 C alters the paste microstructure in regard to the texture of hydration products, the interfacial bond, as well as chemical stability of the microspheres. The first two effects are clearly demonstrated on Figs. 7c and 8b, in which the fractured surface displays open -spheres with smooth cut across their glass shell and the matrix. This observation qualitatively indicates a higher interfacial toughness as compared to samples cured at 20 C. Moreover, a higher degree of -spheres confinement may be expected due to additional fraction of pozzolanic C-S-H, which efficiently fills the free volume and leads to near complete elimination of the capillary pores. Finally, SEM micrographs reveal rare occurrence of local dissolution of microspheres (Fig. 7d), and the formation of new product with fibrillar, or lath-like morphology.

3.4.2. X-ray micro-computed tomography (CT)

Results of the statistical analysis of reconstructed microstructure are presented in Table 4. Overall, the large microscopic voids, which are typical of the air entrapped in the paste during homogenization and consolidation stage, account for less than 3% of the total bulk volume.

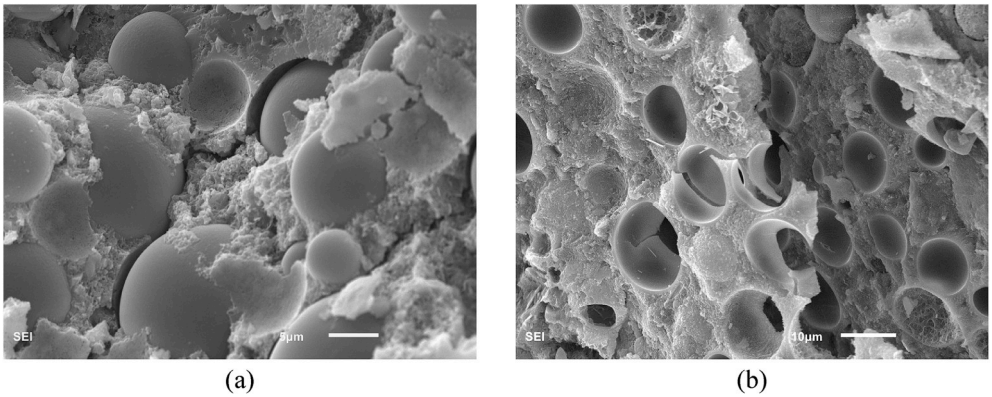

Fig. 8. Micrographs of developed crack after uniaxial compression tests in T2 (Class G): (a) 7 days sample prior to hydrothermal curing, (b) after hydrothermal curing.

Table 3
Measured bulk dry density, (kg/m^3), and open porosity (%), of T1 lightweight cement system.

Sample	P								
	20 C saturated curing			175 C hydrothermal curing (24hr)					
	7 d	14 d	28 d	I	II	III			
(kg/m^3)	915 5*	933 16	936 2	923 3	934 5	922 21			
(%)**	27.7 0.5*	28.7 1.2	27.2 1.5	29.3 0.7	28.3 0.9	28.9 1.8			

* - one standard deviation, ** - estimated from the total evaporable water content.

Table 4
Estimated volume fractions of large microscopic air-voids (f_{mav}), hollow glass -spheres (f_{hs}), and the survival rate (SR) of glass microspheres in the lightweight T1 paste cured for 7 days at room temperature and followed by hydrothermal curing at 175 C.

Sample	f_{mav} (%)		f_{hs} (%)		SR** (%)	
T1 (normal curing)	2.6	0.8*	42.9	0.9	98.1	0.3
T1 (hydrothermal)	1.7	0.7	40.5	0.8	82.8	3.5

* - one standard deviation, ** - defined as the volume fraction of hollow glass microspheres which did not infiltrate with iodine solution.

Moreover, the hollow spheres account for 43% and 41% of the volume of the paste cured in standard and hydrothermal conditions, respectively. This image-based estimates are slightly below the upper bound value of 47%, which is calculated from slurry design parameters (see Table 1) assuming 0% of entrapped air content. If the correction for the entrapped air is made, the existing discrepancy decreases, but still, the CT analysis tends to underestimate the volume fraction occupied by hollow spheres by up to 5% absolute. Both, the low phase contrast between C-S-H based matrix and glass spheres, as well as relatively coarse working resolution (0.74 m/pix), have negative impact on the deconvolution/segmentation process, and are responsible for the observed discrepancy.

In the normally cured paste, the survival rate (SR) of hollow glass -spheres prior to the hydrothermal processing reaches 98%, Table 5. Such high value of SR factor indicates low impact of high-shear mixing of the paste on the microsphere breakage. On the other hand, the hydrothermal processing at 175 C decreases SR value to 83%. This significant reduction is attributed to thermally accelerated glass dissolution mediated by high-ionic strength pore solution. Therefore, the borosilicate spheres contribute partially to the pozzolanic processes despite highly abundant source of SiO^4 (aq), in the form of crystalline micro-silica, incorporated in T1 cement system (see Table 1). Consequently, around one fifth of the initial closed porosity provided by glass bubbles is compromised and open to fluid infiltration (Fig. 9).

Finally, it is interesting to focus on the spatial distribution of regions showing the compromised glass bubbles. While in the normally-cured sample the infiltration of damaged spheres with iodine solution was very rare, with no preference with regard to the spatial location within the microstructure, a specific pattern emerges in the hydrothermally cured paste. In the latter, the regions with high concentration of compromised spheres are located in the very close proximity to entrapped air voids (see Fig. 10), or clusters of unreacted clinker grains. A similar trend has been observed in the SEM investigation discussed previously.

3.5. Thermal conductivity

Results of thermal conductivity assessment are presented in Table 5. Normally cured lightweight T1 cement system displays the average k (W/mK) around 0.28. Given the magnitude of the experimental error in the current analysis, thermal conductivity tends to be unaffected by the sample age. A significant decrease in thermal conductivity is achieved after hydrothermal processing. For T1systems k experiences a reduction of around 12%, relative to its value in the room temperature cured samples. In both cases, lightweight cement system discussed here outperforms normal density Class G paste, T2, for which k 0.64 0.004 W/mK in the dried state and increases to 1.05 0.1 W/mK when saturated.

3.6. Compressive strength

Unconfined compressive strength results are presented in Fig. 11. Samples cured in saturated conditions at normal temperature display the usual trend typical for hydrating cement systems: strength increases with the sample age (degree of hydration). Moreover, as the hydration progresses cement paste becomes more brittle. The 28 days compressive strength is significantly above the minimum required of 17 MPa specified by ACI for lightweight structural concrete [26], and it has been achieved at more than 30% density reduction.

On the other hand, hydrothermal curing at 175 C significantly increases the compressive strength (Fig. 11a). The largest improvement is observed for 7 days old sample, in which the strength is more than doubled. In all cases, this improvement is a direct consequence of thermally activated pozzolanic processes resulting in more refined pore morphology dominated by gel pores, complete elimination of the capillary voids, as well as improved interfacial properties between C-S-H matrix and hollow glass -spheres. Interestingly, the duration of precuring period prior to the hydrothermal treatment does not impact the ultimate strength. Finally, when compared to normally-cured specimens, hydrothermally-cured pastes are more brittle in nature with sudden and abrupt point of failure at the ultimate load.

4. Discussion

4.1. Building lightweight load bearing microstructures with hollow glass -spheres

Based on the presented experimental results, the following guiding principles revolving around the system chemistry, phase thermodynamic stability, and solids packing fraction, are discussed in the context of building lightweight load bearing cement-based matrices and enhanced zonal insolation in HT environments.

4.1.1. System chemistry and thermodynamic phase stability

Under normal conditions hydration of oil well Portland cement results in the formation of nearly amorphous C-S-H gel with molar ratio Ca/Si 1.7 1.8 [22,23]. Precipitating in the pore solution saturated

Table 5
Thermal conductivity of lightweight T1 paste measured in dry state.

Sample	k (W/mK)											
	20 C saturated curing						175 C hydrothermal curing (24hr)					
	7 d		14 d		28 d		I		II		III	
T1 (lightweight)	0.279	0.003*	0.279	0.005	0.286	0.003	0.249	0.003	0.252	0.007	0.241	0.006

* - one standard deviation.

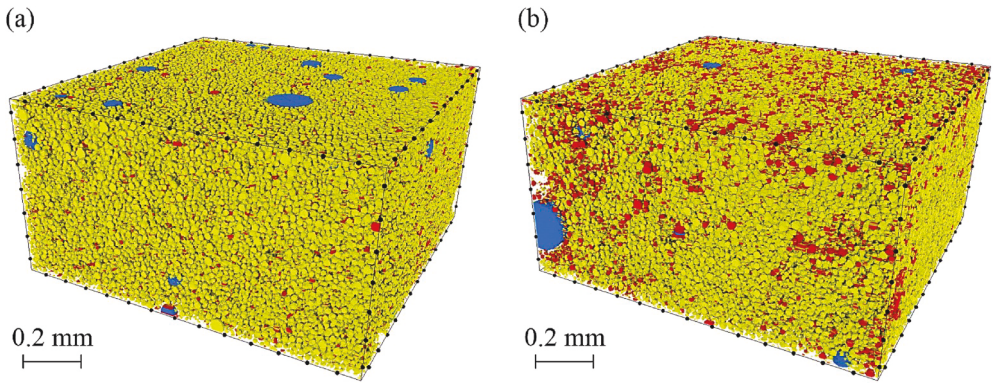

Fig. 9. 3D spatial distribution of hollow glass microspheres and entrapped air voids in the lightweight cement paste cured at 20 °C (a) followed by hydrothermal curing at 175 °C (b). Undisturbed glass spheres presented in yellow, reacted spheres infiltrated with iodine solution presented in red, entrapped air voids in blue. (For interpretation of the references to colour in this figure legend, the reader is referred to the Web version of this article.)

with respect to CH (pH ≈ 12.5), 5-nm thick C-S-H particles have lamellar structure with high specific surface area [70], surface charge density between 0.08 and 0.68 C/m^2 [71,72], both of which control cohesion of the cement system. Although metastable with respect to crystalline calcium silicate phases, C-S-H is persistent in concrete microstructure at normal temperatures [22,73]. However, when the gel is subject to elevated and high temperature, for example in deep wells, thermally enhanced oil recovery wells, or even during accelerated concrete curing at precast plants, it anneals [73] and crystallizes to lower free energy phases e.g. α-dicalcium silicate hydrate (α-C_2SH), and 11 Å tobermorite [47,65,66,74,75]. Whether the C-S-H crystallization is beneficial, or detrimental, to the cementitious matrix is governed by initial Ca/Si ratio of the starting composition [47,76], processing temperature [47,66], and the micro-texture of cement paste prior to accelerated curing [46]. In this regard, possible candidates for the main building block of binding matrix in normal and lightweight systems include xonotlite, 11 Å tobermorite (crystalline and semi-crystalline gel), and gyrolite. Listed calcium silicate hydrates have Ca/Si ≤ 1 [77]. They offer attractive micro texture characteristics e.g. phase morphology of tobermorite, which can be tailored via pore-solution chemistry. Moreover, their molecular framework provides them with particle mechanical properties which are comparable, or even superior, to the properties of regular C-S-H [24,78,79]. However, in the xonotlite phase the water is present in the form of hydroxyl ions only (OH^-) resulting in specific gravity of 2.70 [77], therefore, the effect of its crystallization from C-S-H gel precursor is the net chemical shrinkage and increased capillary porosity of cement matrix. This phase also requires higher temperatures to crystalize (in general above 200 °C) under hydrothermal conditions. In contrary, 11 Å tobermorite and gyrolite display specific gravity 2.46 and 2.45, respectively, due to incorporation of water molecules in their molecular structure. These values are lower than the specific gravity of solid C-S-H nano-particle, 2.604 (H/S = 1.8) [23], indicating potential for more efficient capillary space filling. Moreover, in highly confined environment with limited free volume e.g. high packing density systems, the crystal growth tends to be inhibited and the rate of pore space coarsening (an increase in capillary porosity at the expense of gel pores) can be reduced [46]. Therefore, the design of durable cement systems for enhanced zonal insolation should target the compositional domain and processing conditions of low-lime nano-crystalline calcium silicate hydrates.

This is achieved by adjusting the bulk Ca/Si of the cement mix to be in the range 0.6–1.0 (low-lime CSH type stoichiometry) with reactive source of SiO^{4-} (aq.) in the form of crystalline or amorphous micro-silica. The required reactive silica-to-cement ratio (m_s/m_c) can be calculated according to:

$$\frac{m_s}{m_c} = \frac{\mathscr{M}_c^{Ca} - \beta \mathscr{M}_c^{Si}) \mathscr{M}_{Si}}{\beta} \quad (1)$$

where β is the target Ca/Si ratio of the mix, $\mathscr{M}_c^{Ca}$ and $\mathscr{M}_c^{Si}$ are molar content of CaO and SiO_2 in cement, and $\mathscr{M}_{Si} = 60.08$ g/mol corresponds to molar mass of silicon dioxide, respectively. For example, for Class G (Lafarge-Holcim) used in this study $\mathscr{M}_c^{Ca} = 1.120 \times 10^{-2}$ mol/g, $\mathscr{M}_c^{Si} = 0.355 \times 10^{-2}$ mol/g, which for the design value of β = 0.75 sets m_s/m_c to 0.68. This value of β has been prescribed in the lightweight system investigated here (see Table 1) and it has been calculated assuming micro-quartz (MIN-U-SIL 5) as the primary source of reactive silica. Results of x-ray diffraction (Fig. 4) confirmed the formation of semi-crystalline calcium silicate hydrate in the cementitious matrix which was hydrothermally cured at 175° for 24hrs. This semi-amorphous gel is

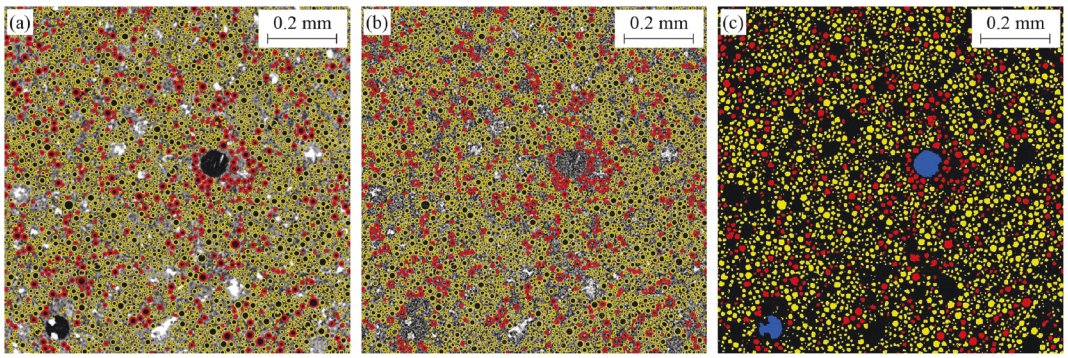

Fig. 10. Contrast enhanced μCT cross sectional analysis of T1 cement system after hydrothermal curing: (a) dry paste, (b) paste saturated with iodine solution, and (c) spatial distribution of dissolved (red) and preserved (yellow) hollow glass μ-spheres with entrapped air microscopic voids (blue). (For interpretation of the references to colour in this figure legend, the reader is referred to the Web version of this article.)

a precursor for crystalline CSH phases which eventually be formed under the conditions of prolonged exposure to thermodynamically favorable conditions in the well environment. On the other hand, the semi-amorphous C-S-H shall persist indefinitely in the matrices of light-weight autoclaved cement systems (AAC) manufactured at T 175 .

4.1.2. Reactive silica source and spheres dissolution

The incorporation of the hollow glass -spheres allows for the reduction of the bulk density of the concrete, as well as introduction of the closed pores into its microstructure. However, to take a full advantage of this technical solution, the chemical and structural stability of the glass shell should not be compromised at any time along the functional lifespan. It should also be stable at the initial stages of system processing e.g. mechanical homogenization and curing. Therefore, minimizing and controlling aqueous glass-corrosion, as well as mechanical damage at the initial stage of material processing, is of importance for discussed lightweight cement systems.

Either in the cement slurry state, or in the hardened paste, hollow glass -spheres are exposed to continuous interaction with pore solution at ionic strengths in the approximate range 0.03 0.29 M and pH-values around 12.5 and above [80]. In aqueous environments the corrosion of silicate glasses arises from several coupled mechanisms: hydration, hydrolysis of the ionic-covalent network and exchange between alkali or alkaline-earth ions and protons in solution [81]. These mechanisms are also present in the dissolution of silicate minerals e.g. quartz. The linear kinetic rate equation, Eq. (2), is commonly used to model basic dissolution process, where c is the instantaneous concentration of the dissolved species, c_0 is the saturation concentration, S is the total available surface area of dissolving solid, V is the solution volume, and r is the dissolution rate constant [82,83].

— – — (2)

Thus, the slowdown of the glass dissolution (corrosion kinetics) can be achieved in two ways: (a) by controlling the saturation of the solution with respect to silica, (b) by decreasing the intrinsic dissolution rate constant, r, via chemical or molecular modifications to glass structure. In practice, a borosilicate glass is the most common commercially available glass type for hollow microspheres used in the industry e.g. iMK30 (3 M). An increased cost associated with the production of more durable glasses is of significant barrier in implementation of the latter solution. However, the chemical affinity route seems to offer an attractive alternative. In this solution the additional source of reactive silica, which will be able to supply SiO^4 (aq.) at the overall rate much higher than the glass -spheres, should be introduced into the cement system. This original approach was tested in the current work by introducing microcrystalline quartz of significantly smaller particle size as compared to the average size of hollow spheres (Table 1). Given its fine diameter, d_{50}

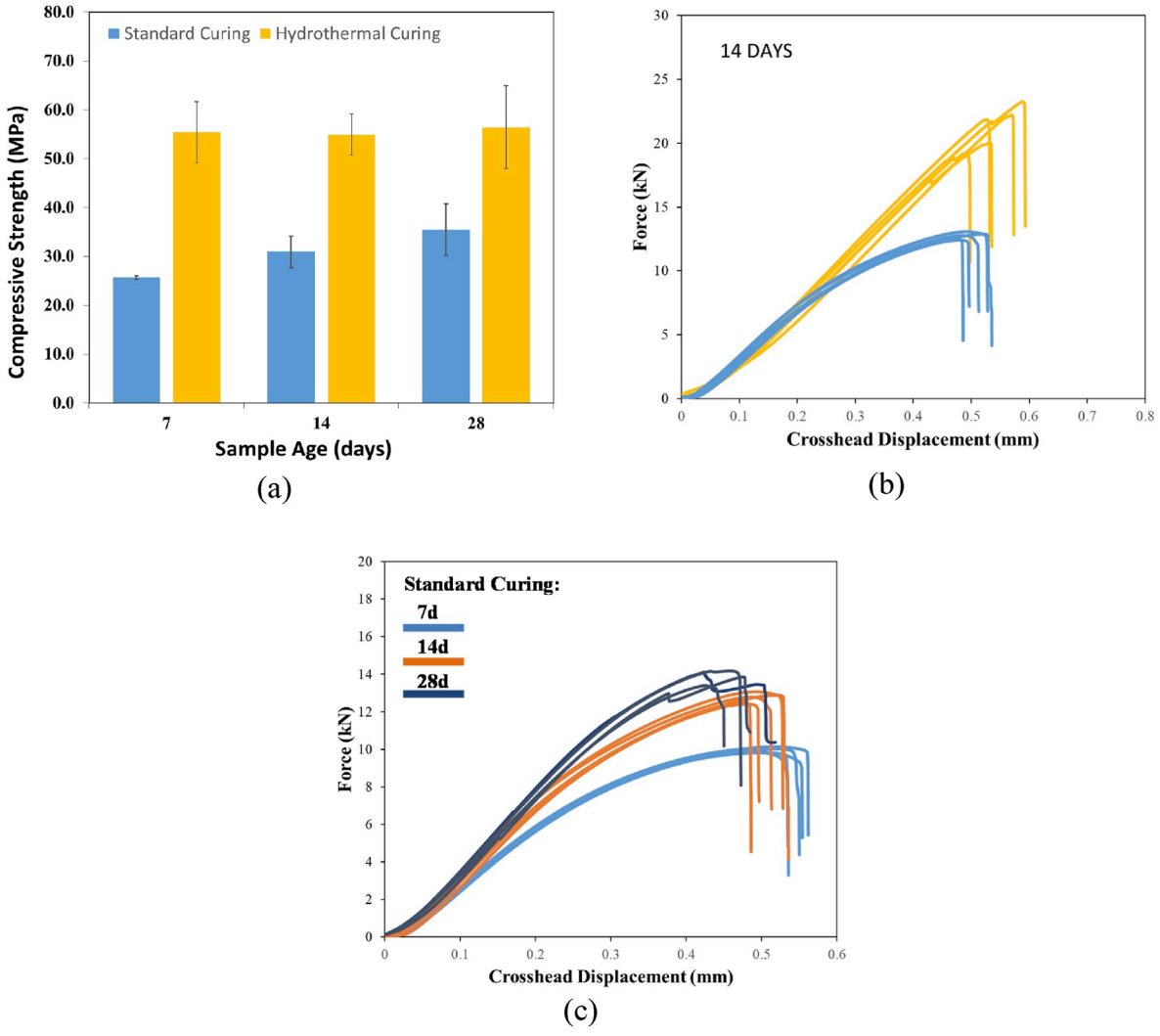

Fig. 11. Effect of curing age (a) and curing conditions (b) on the unconfined compressive strength the investigated cement system, (c) force-displacement diagrams for normally cured samples from 7 to 28 days.

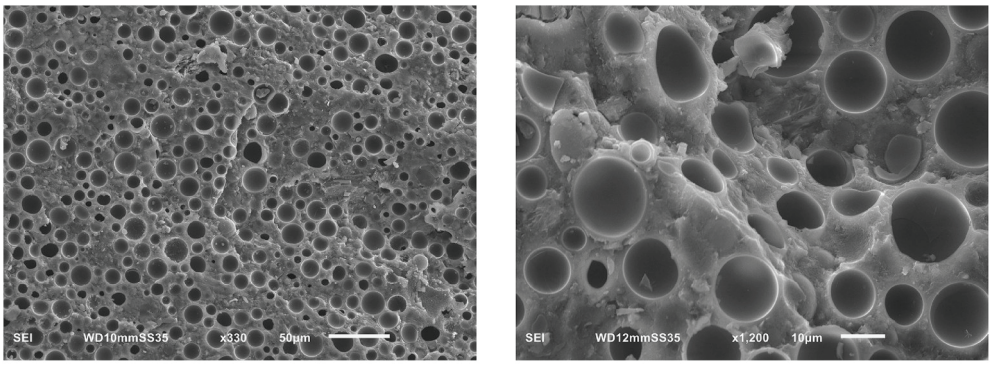

Fig. 12. Secondary electron micrographs of fractured surfaces in the lightweight cement system T1 enriched with silica fume ($\beta_{sf} = 0.29$, $m_w/m_{solids} = 0.2$) and hydrothermally cured at 175° for 24 h. Exposed glass bubbles show sound and continuous glass shell with clear interior embedded in high density composite matrix of C-S-H, crystalline quartz and possibly residual silica fume.

= 1.5 μm, and the specific surface SSA = 1.5 m^2/g, micro-quartz provides almost 72% of the total available surface of reactive silica in the mix. Moreover, due to its fine size it fills space vacancies resulting from packing of glass bubbles and cement particles, hence, serving as a homogenously distributed point sources of SiO^{4-} (aq.) within the matrix. The microstructural investigation with electron microscopy (Figs. 7 and 8), together with X-ray μCT (Figs. 9 and 10), showed that introduction of fine crystalline quartz powder helps in chemical stabilization of glass bubbles. Supported with the x-ray diffraction data (Fig. 4), obtained results indicate an active role of micro-quartz in the thermally activated pozzolanic processes, which would otherwise be entirely consuming SiO^{4-} (aq.) from dissolution of hollow glass μ-spheres. Though being quite effective, it did not eliminate it completely. The estimated survival rate of microspheres, after hydrothermal processing at 175 °C, is round 80% (see Table 4). It must be remembered, this estimate was established for 24hrs curing period (Table 1), which may not be enough to attain thermodynamic equilibrium. Therefore, a further reduction in survival rate should not be excluded in case of prolonged exposure. Studies investigating longer exposure times are currently underway.

Finally, it is plausible the significant mismatch in the intrinsic solubility of silicate glasses and crystalline silica is at the origin of compromised fraction of spheres. Indeed, the difference of almost three orders of magnitude in the dissolution rates separates these two solids [84,85]. Thus, quartz substitution, or augmentation of cement system with amorphous silica additive such as silica fume should have even more positive effect on preservation of hollow μ-spheres. This industrial byproduct [86], has dissolution rate constant, r_{sf}, of a silicate glass, fine particle size with the average diameter of about 100 nm [86] and high specific surface area (SSA) of about 20 m^2/g. In this case, the first order estimate of the required amount of silica fume can be derived based on the modified Eq. (2) taking into account tri-component dissolution process, Eq. (3):

$$\frac{dc}{dt} = \frac{S}{V}\left(f_{hs}r_{hs} + f_{sf}r_{sf} + f_s r_s\right)\left(1 - \frac{c}{c_0}\right) \tag{3}$$

where f_{hs}, f_{sf}, f_s are surface fractions of hollow spheres, silica fume and crystalline silica, respectively, S is the total available surface of reactive silica. After substituting specific surface and weight of each component for surface fraction terms e.g. $f_{hs} = SSA_{hs} \cdot m_{hs}$, Eq. (3) takes the form:

$$\frac{dc}{dt} = \frac{1}{V}\left(SSA_{hs}m_{hs}r_{hs} + SSA_{sf}m_{sf}r_{sf} + SSA_s m_s r_s\right)\left(1 - \frac{c}{c_0}\right) \tag{4}$$

It is apparent, each term in the parenthesis represents the contribution of corresponding silica source to the overall initial dissolution rate. Therefore, to minimize the contribution of glass bubbles to the overall dissolution rate it is required that:

$$\frac{SSA_{sf}m_{sf}r_{sf} + SSA_s m_s r_s}{SSA_{hs}m_{hs}r_{hs}} \gg 1 \tag{5}$$

which after neglecting the second term in the numerator ($SSA_{sf}m_{sf}r_{sf} \gg SSA_s m_s r_s$), and introducing the silica fume-to-cement ratio, β_{sf}, reduces to the following condition.

$$\beta_{sf} \gg \beta_{hs}\frac{\rho_{sf}}{\rho_{hs}}\frac{d_{sf}}{d_{hs}} \tag{6}$$

Given the density and particle diameter ratios, 3.7 and 6.7×10^{-3}, respectively, this condition implies β_{sf} factor to be at least 0.2 for T1 concrete mix (see Table 1). The results of our preliminary investigation (see Fig. 12) of lightweight concrete formulations incorporating crystalline quartz and silica fume suggest increased survival rate of glass bubbles after hydrothermal curing as compared to cement systems with crystalline micro quartz only.

4.1.3. System packing, free volume and paste properties

Packing density of the solids must be considered at the design stage of cement slurry. This factor, which relates to packing of the reactive and non-reactive solids, as well as the subsequent precipitation of the hydration products, is vital for achieving high-specific strength cementitious composite. In particular, the contribution of capillary pores should be considered as they are the primary microstructural features negatively affecting mechanical performance [25]. On the other hand, they positively contribute to lowering thermal conductivity of the porous solid.

According to technical specifications, the median particle size of cement Class G is $d_{50,C} = 30$ μm [64]. This size is comparable to the median size of hollow glass μ-spheres, $d_{50,HS} = 20$ μm [43]. Therefore, it may be assumed that the binary mixture of both coarse particles is close to the maximum packing efficiency of $\eta = 64\%$, which corresponds to random dense packing of mono-sized spheres [87]. Consequently, packing of the coarse material dictates the amount of the interstitial space available to fine micro-silica, which has the median diameter $d_{50,S} = 1$ μm $\ll (d_{50,C}, d_{50,HS})$. Similar to the coarse fraction, the fine micro-silica material packs at the similar efficiency (see Fig. 13a). In this simplified geometrical model, the remaining volume is occupied by water, and its amount is calculated according to:

$$m_w = \left[\frac{(1-\eta)}{\eta}\left(\frac{m_{hs}}{\rho_{hs}} + \frac{m_c}{\rho_c}\right) - \frac{m_s}{\rho_s}\right]\rho_w \tag{7}$$

where m_{hs}, m_c, m_s are the weights of hollow glass μ-spheres, cement, and

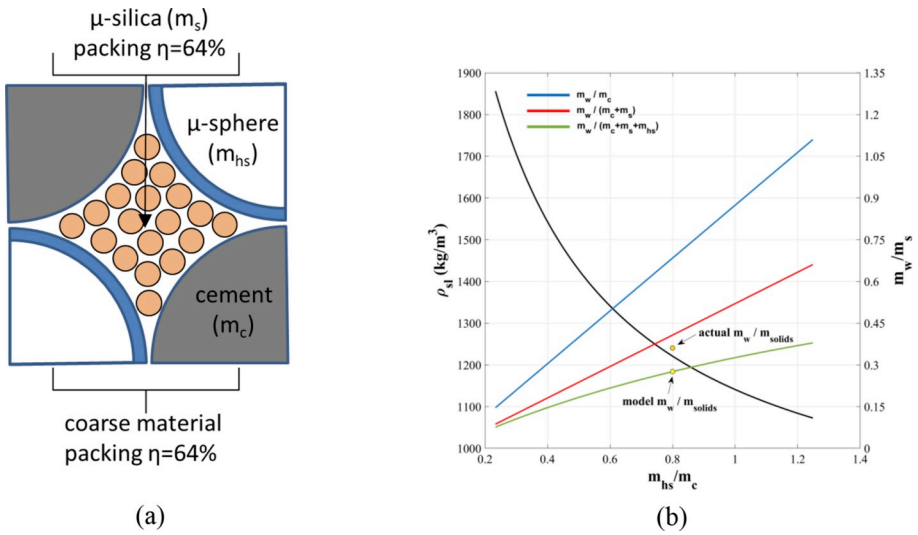

Fig. 13. Simplified thought model of space filling with bimodal PSD (a), variation of the slurry density and water-to-solids ratio in the function of the content of hollow -spheres.

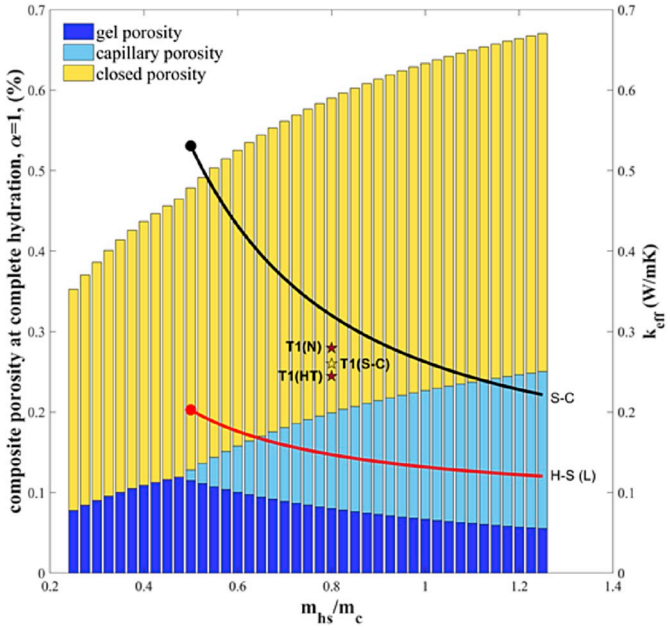

Fig. 14. Gel, capillary, closed porosity and effective thermal conductivity of the lightweight cement system in the function of -spheres content per unit weight of cement. Values estimated under assumption of complete hydration. T1(N) and T1(HT) refer to normal (20 C, saturated) and hydrothermal curing (175 C) of investigated lightweight composite. Notice, the total open porosity in T1 system is 28% (Table 3).

micro-silica, respectively. Naturally, for fixed cement and silica content the slurry density decreases with increasing number of hollow micro-spheres, Fig. 13b. On the contrary, the water-to-solid ratio increases as there is more free volume available for water. However, given the very large fineness of the mix component, the calculated amount of water, m_w, may not be enough to provide the mix with the sufficient work-ability characteristics. Therefore, the required amount of additional water supplemented with the water reducing admixture can be adjusted in the trial mixture to provide adequate rheology. For example, in the present study, the theoretical water-to-solids ratio of T1 system is 0.28, however, the adjusted value which results in the adequate flow is 0.36 (see Fig. 13b, Table 1). As a consequence, the slurry density and solid

Table 6
Volumetric thermal conductivity and density values of hydrated T1 cement system components.

Sample	Phase					
	C_3S	Quartz	-spheres	C1.75-S-H2.0	CH	Air
(g/cm^3)	3.12	2.65	0.6	2.6¥	2.24	
k (W/mK)	3.35**	7.7*	0.187	0.98**	1.32**	0.024

* - effective thermal conductivity, k_{eff} $\frac{1}{3}k$ $\frac{2}{3}k$.
Where k 10.7 W/mK and k 6.2 W/mK [91], ** - after [24], ¥ - after [23], - after [22].

packing decreases to 1204 kg/m^3 and 68%, respectively (model density 1221 kg/m^3, 74% packing).

Given the proportions of each particulate ingredient the effect of hollow spheres content on the thermal conductivity of the hydrated cement paste can be inferred. From now onward, it is assumed that cement is composed of C_3S phase only, its hydration reached an asymptote (1), and micro-quartz together with glass -spheres are chemically inert. The classic Powers-Brownyard [22,88] model is employed to estimate the gel and capillary porosity in the hydrated cement paste (Fig. 14), while mass balance equation of C_3S hydration is used to estimate the weight fractions of hydration products, $C_{1.7}$-S-$H_{2.0}$ and CH [34]. The effective thermal conductivity of the lightweight cement composite is represented as the Hashin-Shtrikman (H-S) lower bound [89] and self-consistent (S-C) approximation [90] (Fig. 14), both of which were calculated assuming the intrinsic phase properties detailed in Table 6.

Despite the significant simplifications of the model, the valid trends can be inferred and used as an initial guideline in the design of the lightweight cement systems similar to the ones investigated in this work. Therefore, the increasing concentration of the -spheres in the cement slurry results in increased total porosity, the sum of gel and capillary voids, respectively. Such trend is a direct consequence of the pre-fixed amount of the micro-quartz and increasing free volume. This trend is followed by the effective thermal conductivity, k, for which both effective estimates steadily reduce with rising m_{hs}/m_c (Fig. 14). Moreover, the experimentally measured thermal conductivities of T1 pastes (Table 5), normal and hydrothermally cured, are within the domain set by H-S lower bound and S-C estimates derived based on the introduced simplified model. In fact, after accounting for 10% divergence in the

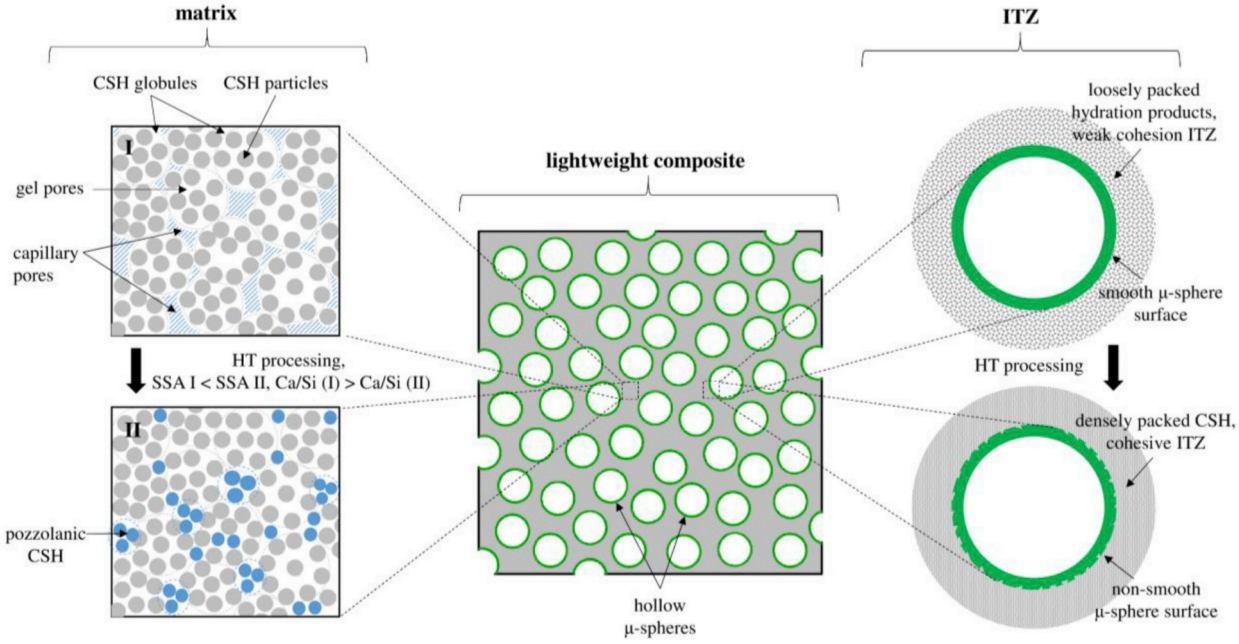

Fig. 15. Summary schematic of the effect of hydrothermal treatment of the textural changes of the lightweight cement composite matrix and ITZ. For clarity matrix is represented by its principal phases, C-S-H and CH.

total open porosity from the model value, both, C-S estimate and experiment show close agreement.

With regard to the strength of investigated lightweight composites, although beneficial from the standpoint of thermal properties, the incorporation of the hollow spheres in increasing amounts results in the lower gel/space ratio and capillary porosity. Moreover, the weak ITZ with low interfacial toughness between cementitious matrix and glass -spheres has been observed (see Fig. 7a and b and Fig. 8a). Therefore, a strength decline should be expected for normally cured pastes with increasing m_{hs}/m_c ratio [10,22,92]. However, still in case of investigated lightweight system, in which -spheres constitute 80% by weight of cement (around 47% by paste volume) the 28days compressive strength of 36 MPa was achieved, which is significantly above the minimum required for the structural lightweight concrete [26]. More importantly, the load-bearing capacity of the material has drastically improved after accelerated curing in the hydrothermal conditions; more than 50% improvement (see Fig. 11) achieved at similar value of total porosity. This significant increase in the load bearing capacity is caused by the textural changes in the matrix phase and ITZ which are schematically depicted in Fig. 15. These changes refer to: a) altering mineralogy and composition of the matrix as discussed in the previous sections, b) pore space refinement with close to complete elimination of

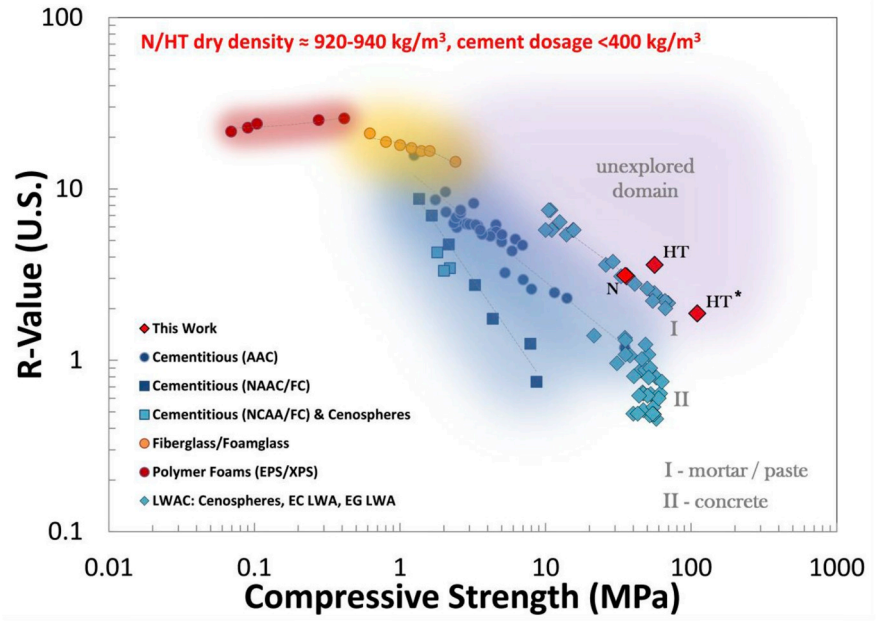

Fig. 16. Map of thermal resistance vs. compressive strength of lightweight cement systems. R-values (U.S.) are calculated for 15.24 cm (6) barrier thickness, SI R-Value 0.176 R.Value (U.S.) conversion applies. N/HT refers to T1 cement system cured in normal (N) and hydrothermal (HT) conditions, HT* preliminary data for T1 composite enriched with silica fume ($_{sf}$ 0.29, m_w/m_{solids} 0.2). Literature data after [4 21].

the capillary voids and c) enhancement of the interfacial toughness of ITZ.

4.2. Thermo-mechanical metrics and cement dosage

In the selection of the optimum slurry design for oil-gas-geothermal wells cement liner, or lightweight concrete, mechanical strength, thermal conductivity and density are key metrics considered. Naturally, the high specific strength cement-based composite with the high insulation potential is desirable. Moreover, given the environmental footprint of the OPC, it is beneficial if listed metrics can be achieved at the reduced cement content. Certainly, high strength hollow glass -spheres systems offer new opportunities in this area as shown by the results of this research and others (Fig. 16).

Among recent developments, Wu et al. [11] reported on high specific strength ultra-lightweight cement composites in the dry density range 970 1300 kg/m^3 for which cenosphere content varied from 270 to 440 kg/m^3 (38 52% by volume) of the slurry. As expected, the strength values of up to 60 MPa with *k* of 0.4 W/mK were obtained at the upper density range. On the other hand, strength of 33 MPa and *k* of 0.28 were achieved for oven dry density of 970 kg/m^3. However, it is worth to notice that the corresponding mix designs heavily rely on the substantial quantity of OPC, which ranges from 500 to 850 kg/m^3 of mix, to boost mechanical performance. The experimental results outlined in the current work show that lightweight cement composites with similar, or even greater mechanical and thermal characteristics can be achieved at the lower cement dosage (Fig. 16). Moreover, if subject to different curing conditions e.g. hydrothermal in the high depth wells or autoclaving at the precast plant, the specific strength can be drastically enhanced without compromising on density or thermal conductivity (Tables 3 and 5); 60% strength enhancement was recorded for T1 system (see Fig. 11). It is of author s opinion, that lightweight cement composites with even greater specific strength and lower thermal conductivity should be attainable at low cement dosage by tailoring the composition-microstructure-processing link, similarly to what have been achieved in the area of high (HPC) and ultra-high (UHPC) performance concrete.

5. Summary and Conclusions

This work explored different aspects of mix design, processing and microstructure engineering of silica-enriched light-weight oil-well cement systems with hollow glass -spheres for high specific strength and reduced thermal conductivity in cement liners operating in normal and HTHP environments. For this purpose, the model lightweight cement composite has been synthesized and characterized with various experimental methods to infer changes in matrix mineralogy, texture, as well as physical and mechanical properties. The effect of silica doping and hydrothermal treatment on the structural and chemical stability of hollow glass spheres was assessed with x-ray tomography and the survival rates were estimated. Moreover, supported with the experimental data the discussion of the effect of system chemistry and solids packing on the matrix composition, spheres dissolution and thermo-mechanical performance was presented.

The experimental analysis revealed the beneficial effect of silica additive on the chemical stability of the glass spheres. Although close to inert in the room temperature cured pastes, hollow -microspheres will take an active role in the thermally activated pozzolanic processes if no other significant silica source is present. However, the selection of the auxiliary siliceous additive should be guided by the additive specific surface area (SSA) as well as its dissolution rate constant (r). Although not completely eliminated, the glass corrosion processes can be substantially inhibited enhancing the endurance of the -spheres in the cement-based matrix, thus preserving the closed porosity and strengthening the C-S-H matrix with stiff and hard glass shell. The application of the crystalline micro-silica helps to achieve this effect. However, the estimated survival rate is around 83%, thus close to one fifth of spheres population lost its functionality. As indicated by the preliminary data enrichment with silica fume has potential to increase the survival rate.

The auxiliary silica source (additive) takes the primary role in the pozzolanic processes and phase transformations in which low-lime calcium silicate hydrates, crystalline or semi-crystalline, constitute the matrix hosting hollow spheres. While the pore domain in the normally cured systems spans across broad range of pore sizes, the hydrothermal processing significantly narrows the pore size distribution to gel pores, with close to zero contribution of capillary voids.

Cement composites with hollow glass microspheres, introduced in this study, are capable of delivering load bearing capacity significantly above 17 MPa the minimum required for lightweight structural concrete specified by ACI [26]. It has been shown that hydrothermal curing significantly enhances the specific strength of lightweight composite while preserving its low thermal conductivity, which has been measured 0.28 and 0.24 W/mK, normal and hydrothermally treated pastes, respectively. Experimental measurements are in close agreement to theoretically derived bounds based on the presented simplified model, which can be used as an initial design guideline of systems alike. Moreover, competitive thermo-mechanical metrics have been achieved at lower cement dosage, $<$ 400 kg/m^3 (per meter cube of slurry), as compared with reported data for composites of similar density.

In the author s opinion, lightweight cement composites with even greater specific strength and lower thermal conductivity should be within reach if the particular attention is paid to material aspect at all scales. The presented findings concerned oil-well cement systems, however, given the substantial similarities between oil well cements and typical construction cements, they may be of interest to the precast and calcium silicate insulation industries.

Acknowledgement

This work was supported by the National Science Foundation under Grants No. 1825921. The research team is also grateful Lafarge-Holcim, BASF, Vallourec and 3 M companies for supporting this study.

Appendix A. Supplementary data

Supplementary data to this article can be found online at https://doi.org/10.1016/j.cemconcomp.2020.103514.

References

[1] N.D. Agrawal, Thermal Analysis on Permaforst Subsidence on the North Slope of Alaska, Master Thesis, University of Alaska Fairbanks, 2015.
[2] G. DeBruijn, C. Skeates, R. Greenaway, D. Harrison, M. Parris, S. James, F. Mueller, S. Ray, M. Riding, L. Temple, K. Wutherich, High-pressure, high-temperature technologies, Oilfield Rev. 20 (3) (2008) 46 60.
[3] E.J. Couch, J. Watts, Permafrost thawing around producing oil wells, J. Can. Pet. Technol. 9 (2) (1970).
[4] S. Shahidan, E. Aminuddin, K.M. Noor, N. Raihan, N.I.R.R. Hannan, N.A.S. Bahari, Potential of hollow glass microsphere as cement replacement for lightweight foam concrete on thermal insulation performance, MATEC Web Conf 103 (2017) 1 9, https://doi.org/10.1051/matecconf/201710301014, 01014.
[5] A.J. Hamad, Materials, production, properties and application of aerated lightweight concrete: review, Int. J. Mater. Sci. Eng. 2 (2014) 152 157, https://doi.org/10.12720/ijmse.2.2.152-157.
[6] A.L. Brooks, H. Zhou, D. Hanna, Comparative study of the mechanical and thermal properties of lightweight cementitious composites, Constr. Build. Mater. 159 (20) (2018) 316 328, https://doi.org/10.1016/j.conbuildmat.2017.10.102.
[7] J.A. Rossignolo, M.V.C. Agnesini, J.A. Morais, Properties of high-performance LWAC for precast structures with Brazilian lightweight aggregates, Cement Concr. Compos. 25 (2003) 77 82, https://doi.org/10.1016/S0958-9465(01)00046-4.
[8] F. Blanco, P. Garcia, P. Mateos, J. Ayala, Characteristics and properties of lightweight concrete manufactured with cenospheres, Cement Concr. Res. 30 (2000) 1715 1722, https://doi.org/10.1016/S0008-8846(00)00357-4.
[9] S.L. Sarkar, S. Chandra, L. Berntsson, Interdependence of microstructure and strength of structural lightweight aggregate concrete, Cement Concr. Compos. 14 (1992) 239 248, https://doi.org/10.1016/0958-9465(92)90022-N.

[10] A. Hanif, Z. Lu, Z. Li, Utilization of fly ash cenosphere as lightweight filler in cement-based composites - a review, Constr. Build. Mater. 144 (30) (2017) 373 384, https://doi.org/10.1016/j.conbuildmat.2017.03.188.

[11] Y. Wu, J.-Y. Wang, P.J.M. Monteiro, M.-H. Zhang, Development of ultra-lightweight cement composites with low thermal conductivity and high specific strength for energy efficient buildings, Constr. Build. Mater. 87 (2015) 100 112, https://doi.org/10.1016/j.conbuildmat.2015.04.004.

[12] D. Oreshkin, V. Semenov, T. Rozovskaya, Properties of light-weight extruded concrete with hollow glass microspheres, Procedia Eng 153 (2016) 638 643, https://doi.org/10.1016/j.proeng.2016.08.214.

[13] Q.L. Yu, P. Spiesz, H.J.H. Brouwers, Ultra-lightweight concrete: conceptual design and performance evaluation, Cement Concr. Compos. 61 (2015) 18 28, https://doi.org/10.1016/j.cemconcomp.2015.04.012.

[14] W. Pichor, Properties of autoclaved aerated concretes with cenospheres from coal ash, Cem. Lime Concr. 1 (2012) 32 37.

[15] N. Narayanan, K. Ramamurthy, Structure and properties of aerated concrete: a review, Cement Concr. Compos. 22 (2000) 321 329, https://doi.org/10.1016/S0958-9465(00)00016-0.

[16] K. Kunchariyakun, S. Asavapisit, K. Sombatsompop, Properties of autoclaved aerated concrete incorporating rice husk ash as partial replacement forfineaggregate, Cement Concr. Compos. 55 (2015) 11 16, https://doi.org/10.1016/j.cemconcomp.2014.07.021.

[17] Y. Song, B. Li, E.-H. Yang, Y. Liu, T. Ding, Feasibility study on utilization of municipal solid waste incineration bottom ash as aerating agent for the production of autoclaved aerated concrete, Cement Concr. Compos. 56 (2015) 51 58, https://doi.org/10.1016/j.cemconcomp.2014.11.006.

[18] L. Ropelewski, R.D. Neufeld, Thermal inertia properties of autoclaved aerated concrete, J. Energy Eng. 125 (2) (1999) 59 75, https://doi.org/10.1061/(ASCE)0733-9402 (1999)125:2(59).

[19] K.-H. Yang, K.-H. Lee, Tests on high-performance aerated concrete with lower density, Constr. Build. Mater. 74 (2015) 109 117, https://doi.org/10.1016/j.conbuildmat.2014.10.030.

[20] Foamglas HLB Block Insulation, 2019. https://industry.foamglas.com/en-gb/products/foamglas-hlb-insulation/grades-and-formats/. (Accessed 24 May 2019).

[21] M. Albayrak, A. Yörüko˘glu, S. Karahan, S. Atlıhan, H.Y. Aruntas, I. Girgin, Influence of zeolite additive on properties of autoclaved aerated concrete, Build. Environ. 42 (9) (2007) 3161 3165, https://doi.org/10.1016/j.buildenv.2006.08.003.

[22] H.F.W. Taylor, Cement Chemistry, second ed., Thomas Telford, London, 1997.

[23] A.J. Allen, J. Thomas, H.M. Jennings, Composition and density of nanoscale calcium-silicate-hydrate in cement, Nat. Mater. 6 (2007) 311 316, https://doi.org/10.1038/nmat1871.

[24] M.J.A. Qomi, F.-J. Ulm, R.J.-M. Pellenq, Physical origins of thermal propoerties of cement paste, Phys. Rev. Applied. 3 (2015), 064010, https://doi.org/10.1103/PhysRevApplied.3.064010.

[25] S. Mindes, J.F. Young, D. Darwin, Concrete, second ed., Prentice Hall, 2002.

[26] A. 213R-87, Guide for Structural Lightweight Aggregate Concrete, American Concrete Institute, 1999.

[27] N. Konckal, T. Ozturan, Strength and elastic properties of structural lightweight concretes, Mater. Des. 32 (2011) 2396 2403, https://doi.org/10.1016/j.matdes.2010.12.053.

[28] H. Oktay, R. Yumrutas, A. Akpolat, Mechanical and thermophysical properties of lightweight aggregate concretes, Constr. Build. Mater. 96 (2015) 217 225, https://doi.org/10.1016/j.conbuildmat.2015.08.015.

[29] A.S. Inozemtcev, High-strength lightweight concrete mixtures based on hollow microspheres: technological features and industrial experience of preparation, IOP Conf. Ser. Mater. Sci. Eng. 71 (1) (2015), 012028, https://doi.org/10.1088/1757-899X/71/1/012028.

[30] S.P. McBride, A. Shukla, A. Bose, Processing and characterization of a lightweight concrete using cenospheres, J. Mater. Sci. 37 (2002) 4217 4225, https://doi.org/10.1023/A:1020056407402.

[31] G. Samson, C. Lanos, A. Phelipot-Mardele, A review of thermomechanical properties of lightweight concrete, Mag. Concr. Res. 69 (4) (2017) 201 216, https://doi.org/10.1680/jmacr.16.00324.

[32] R. Gül, E. Okuyucu, I. Türkmen, A. Cüneyt Aydin, Thermo-mechanical properties of fiber reinforced raw perlite concrete, Mater. Lett. 61 (29) (2007) 5145 5149, https://doi.org/10.1016/j.matlet.2007.04.050.

[33] D.P. Bentz, Transient plane source measurements of the thermal properties of hydrating cement pastes, Mater. Struct. 40 (2007) 1073 1080, https://doi.org/10.1617/s11527-006-9206-9.

[34] P.D. Tennis, H.M. Jennings, A model for two types of calcium silicate hydrate in the microstrcutre of Portland cement pastes, Cement Concr. Res. 30 (2000) 855 863, https://doi.org/10.1016/S0008-8846(00)00257-X.

[35] G. Constantinides, F.J. Ulm, The effect of two types of CSH on the elasticity of cement-based materials: results from nanoindentation and micromechanical modeling, Cement Concr. Res. 34 (2004) 67 80, https://doi.org/10.1016/S0008-8846(03)00230-8.

[36] X. Qu, X. Zhao, Previous and present investigations on the components, microstrcture and main properties of autoclaved aerated concrete - a review, Constr. Build. Mater. 135 (2017) 505 516, https://doi.org/10.1016/j.conbuildmat.2016.12.208.

[37] K. Ramamurthy, E. Kunhanandan Nambiar, G. Indu Siva Ranjani, A classification of studeis on properties of foam concrete, Cement Concr. Compos. 31 (2009) 388 396, https://doi.org/10.1016/j.cemconcomp.2009.04.006.

[38] J.-Y. Wang, Y. Yang, J.-Y. Liew, M.-H. Zhang, Method to determine mixture proportions of workable ultra lightweight cement composites to achieve target unit weights, Cement Concr. Compos. 53 (2014) 178 186, https://doi.org/10.1016/j.cemconcomp.2014.07.006.

[39] A.K. Suryavanshi, R.N. Swamy, Development of lightweight mizes using ceramic microspheres as fillers, Cement Concr. Res. 32 (11) (2002) 1783 1789, https://doi.org/10.1016/S0008-8846(02)00871-2.

[40] S. Fickler, B. Milow, L. Ratke, M. Schnellenbach-Held, T. Welsch, Development of high performance aerogel concrete, Energ. Procedia 78 (2015) 406 411, https://doi.org/10.1016/j.egypro.2015.11.684.

[41] Q. Zeng, T. Mao, H. Li, Y. Peng, Thermally insulating lightweight cement-based composites incorporating glass beads and nano-silica aerogels for sustainability energy-saving buildings, Energy Build. 174 (1) (2018) 97 110, https://doi.org/10.1016/j.enbuild.2018.06.031.

[42] S. Ng, B.P. Jelle, L.I.C. Sandberg, T. Gao, O.H. Wallevik, Experimental investigations of aerogels-incorporated ultra-high performance concrete, Constr. Build. Mater. 77 (15) (2015) 307 316, https://doi.org/10.1016/j.conbuildmat.2014.12.064.

[43] 3M, 3M Glass Bubbles. https://www.3m.com/, 2019. (Accessed 24 May 2019).

[44] A.K. Chatterjee, X-ray diffraction, in: V.S. Ramachandran, J.J. Beaudoin (Eds.), Handbook of Analytical Techniques in Concrete Science and Technology: Principles, Tehcniques and Applications, Noyes Publications, William Andrew Publishing, New York, 2001, pp. 275 333.

[45] S. Lowell, J.E. Shields, M.A. Thomas, M. Thommes, Characterization of Porous Solids and Powders: Surface Area, Pore Size and Density, Springer Science Buisness Media, New York, 2004, https://doi.org/10.1007/978-1-4020-2303-3.

[46] K.J. Krakowiak, J.J. Thomas, S. James, M. Abuhaikal, F.-J. Ulm, Development of silica-enriched cement-based materials with improved aging resistance for application in high-temperature environments, Cement Concr. Res. 105 (2018) 91 110, https://doi.org/10.1016/j.cemconres.2018.01.004.

[47] K.J. Krakowiak, J.J. Thomas, S. Musso, A.-T. Akono, F.-J. Ulm, Nano-chemo-mechanical signature of conventional oil-well cement systems: effects of elevated temperature and curing time, Cement Concr. Res. 67 (2015) 103 121, https://doi.org/10.1016/j.cemconres.2014.08.008.

[48] R.F. Feldman, Pore structure damage in blended cements caused by mercury intrusion, J. Am. Ceram. Soc. 67 (1) (1984) 30 33, https://doi.org/10.1111/j.1151-2916.1984.tb19142.x.

[49] R.F. Feldman, J.J. Beaudoin, Pretreatment of hardened hydrated cement pastes for mercury intrusion measurements, Cement Concr. Res. 21 (2) (1991) 297 308, https://doi.org/10.1016/0008-8846(91)90011-6.

[50] E.P. Barrett, L.G. Joyner, P.P. Halenda, The determination of pore volume and area distributions in porous substances: I. Computations from nitrogen isotherms, J. Am. Chem. Soc. 73 (1) (1951) 373 380, https://doi.org/10.1021/ja01145a126.

[51] M. Thommes, K. Kaneko, A.V. Neimark, J.P. Olivier, F. Rodriguez-Reinoso, J. Rouquerol, K.S.W. Sing, Physisorption of gases, with special reference to the evaluation of surface area and pore size distribution (IUPAC Technical Report), Pure Appl. Chem. 87 (9 10) (2015) 1051 1069, https://doi.org/10.1515/pac-2014-1117.

[52] F. Schüth, K.S.W. Sing, J. Weitkamp, Handbook of Porous Solids, Wiley-VCH, Weinheim, 2002, https://doi.org/10.1002/9783527618286.

[53] J. Zhang, G.W. Scherer, Comparison of methods for arresting hydration of cement, Cement Concr. Res. 41 (10) (2011) 1024 1036, https://doi.org/10.1016/j.cemconres.2011.06.003.

[54] M.C. Garci Juenger, H.M. Jennings, The use of nitrogen adsorption to assess the microstrcture of cement paste, Cement Concr. Res. 31 (2001) 883 892, https://doi.org/10.1016/S0008-8846(01)00493-8.

[55] H. Lusic, M.W. Grinstaff, X-ray-computed tomography contrast agents, Chem. Rev. 113 (3) (2012) 1641 1666, https://doi.org/10.1021/cr200358s.

[56] X. Wang, D. Meier, K. Taguchi, D.J. Wagenaar, B.E. Patt, E.C. Frey, Material separation in x-ray CT with energy resolved photon-counting detectors, Med. Phys. 38 (3) (2011) 1534 1546, https://doi.org/10.1118/1.3553401.

[57] L.A. Feldkamp, L.C. Davis, J.W. Kress, Practical cone-beam algorithm, J. Opt. Soc. Am. A 1 (1984) 612 619, https://doi.org/10.1364/JOSAA.1.000612.

[58] M. Kuwahara, K. Hachimura, S. Eiho, M. Kinoshita, Processing of RI-angiocardiographic images, in: K. Preston, M. Onoe (Eds.), Digital Processing of Biomedical Images, Springer, Boston, 1976, pp. 187 202, https://doi.org/10.1007/978-1-4684-0769-3_13.

[59] K. Bartyzel, Adaptive Kuwahara filter, sig. Image vid, Process 10 (4) (2016) 663 670, https://doi.org/10.1007/s11760-015-0791-3.

[60] ASTM C518-04 Standard Test Method for Steady-State Thermal Transmission Properties by Means of the Heat Flow Meter Aparatus, ASTM, 2004.

[61] ASTM E 1530-06 Standard Test Method for Evaluating the Resistance to Thermal Transmission of Materials by the Guarded Heat Flow Meter Technique, ASTM, 2006.

[62] A. Brzezinski, A. Tleoubaev, Effects of interface resistance on measurements of thermal conductivity of composites and polymers, in: K.J. Kociba (Ed.), Proceedings of the 30th Annual Conference on Thermal Analysis and Applications, Pittsburgh, PA, 2002, pp. 512 517.

[63] ASTM C39/C39M-14a Standard Test Method for Compressive Strength of Cylindrical Concrete Specimens, ASTM International, West Conshohocken, PA, 2014.

[64] E.B. Nelson, Well Cementing, second ed., Schlumberger, Houston, 2006.

[65] T. Mitsuda, K. Sasaki, H. Ishida, Phase evolution during autoclaving process of aerated concrete, J. Am. Ceram. Soc. 75 (7) (1992) 1858 1863, https://doi.org/10.1111/j.1151-2916.1992.tb07208.x.

[66] H.F.W. Taylor, The steam curing of Portland cement products, in: H.F.W. Taylor (Ed.), The Chemistry of Cements, Academic Press, London, 1964, pp. 417 432.

[67] G.L. Kalousek, The reactions of cement hydration at elevated temperatures. Proc. 3rd, Internat. Symp. Chem. Cement, London, 1952, pp. 334 367.
[68] C. Hall, W.D. Hoff, Water Transport in Brick, Stone and Concrete, second ed., CRC Press, London, 2009 https://doi.org/10.1201/b12840.
[69] H.M. Jennings, Refinements to colloid model of C-S-H in cement: CM-II, Cement Concr. Res. 38 (3) (2008) 275 289, https://doi.org/10.1016/j.cemconres.2007.10.006.
[70] J.J. Thomas, H.M. Jennings, A.J. Allen, The surface area of hardened cement paste as measured by various techniques, Concr. Sci. Eng. 1 (1999) 45 64.
[71] C. Plassard, E. Lesniewska, I. Pochard, A. Nonat, Nanoscale experimental investigation of particle interactions at the origin of the cohesion of cement, Langmuir 21 (2005) 7263 7270, https://doi.org/10.1021/la050440 .
[72] R.J.-M. Pellenq, N. Lequex, H. van Damme, Engineering the bonding scheme in C-S-H: the iono-covalent framework, Cement Concr. Res. 38 (2) (2008) 159 174, https://doi.org/10.1016/j.cemconres.2007.09.026.
[73] F. Glasser, Cements in Radioactive Waste Disposal, International Atomic Energy Agency.
[74] S. Shaw, C.M.B. Henderson, S.M. Clark, In-situ synchrotron study of the kinetics, thermodynamics, and reaction mechanisms of the hydrothermal crystallization of gyrolite, Ca16Si24O60(OH)8 14H2O, Am. Mineral. 87 (4) (2002) 533 541, https://doi.org/10.2138/am-2002-0416.
[75] S.A.S. El-Hemaly, T. Mitsuda, H.F.W. Taylor, Synthesis of normal and anomalous tobermorite, Cement Concr. Res. 7 (4) (1977) 429 438, https://doi.org/10.1016/0008-8846(77)90071-0.
[76] C.A. Menzel, Strength and volume change of steam cured concrete, J. Proc. 31 (11) (1934) 125 148.
[77] I.G. Richardson, The calcium silicate hydrates, Cement Concr. Res. 38 (2) (2008) 137 158, https://doi.org/10.1016/j.cemconres.2007.11.005.
[78] G. Geng, R. Myers, M. Abdolhosseinin Qomi, P. Monteiro, Densification of the interlayer spacing governs the nanomechanical properties of calcium-silicate-hydrate, Sci. Rep. 7 (2017), 10986, https://doi.org/10.1038/s41598-017-11146-8.
[79] H. Manzano, Atomistic Simulation Studies of the Cement Paste Components, Universidad del Pais Vasco, 2009.
[80] K. Andersson, B. Allard, M. Bengtsson, B. Magnusson, Chemical composition of cement pore solutions, Cement Concr. Res. 19 (3) (1989) 327 332, https://doi.org/10.1016/0008-8846(89)90022-7.
[81] C. Cailleteau, F. Angeli, F. Devreux, S. Gin, J. Jestin, P. Jollivet, O. Spalla, Insight into silicate-glass corrosion mechanisms, Nat. Mater. 7 (2008) 978 983, https://doi.org/10.1038/nmat2301.
[82] W.L. Bourcier, W.L. Ebert, X. Feng, Modeling surface area to volume effects on borosilicate glass dissolution, MRS Proc 294 (1992) 577, https://doi.org/10.1557/PROC-294-577.
[83] A. Dokoumetzidis, P. Macheras, A century of dissolution research: from noyes and whitney to the biopharmaceutics classification system, Int. J. Pharm. 321 (1 2) (2006) 1 11, https://doi.org/10.1016/j.ijpharm.2006.07.011.
[84] I. Pignatelli, A. Kumar, M. Bauchy, G. Sant, Topological control on silicates dissolution kinetics, Langmuir 32 (18) (2016) 4434 4439, https://doi.org/10.1021/acs.langmuir.6b00359.
[85] S. Nangia, B.J. Garrison, Reaction rates and dissolution mechanisms of quartz as a function of pH, J. Phys. Chem. A 112 (2008) 2027 2033, https://doi.org/10.1021/jp076243w.
[86] S.H. Kosmatka, M.C. Wilson, Design and Control of Concrete Mixtures, sixteenth ed., Portland Cem. Ass., Skokie, 2016.
[87] R.M. German, Particle Packing Characteristics, Metal Powder Industries Federation, Princeton, 1989.
[88] H.J.H. Brouwers, The work of Powers and brownyard revisited: Part I, cem, Concr. Res. 34 (9) (2004) 1697 1716, https://doi.org/10.1016/j.cemconres.2004.05.031.
[89] Z. Hashin, S. Shtrikman, A variational approach to the theory of effective magnetic permeability of multiphase materials, J. Appl. Phys. 33 (1962) 3125 3131, https://doi.org/10.1063/1.1728579.
[90] Y.Z. Benveniste, On the effective thermal conductivity of multiphase composites, J. Appl. Math. Phys. 37 (1986) 696 713, https://doi.org/10.1007/BF00947917.
[91] K.-I. Horat, G. Simmon, Thermal conductivity of rock forming minerals, Earth Planet. Sci. Lett. 6 (5) (1969) 359 368, https://doi.org/10.1016/0012-821X(69)90186-1.
[92] P.K. Mehta, P.J.M. Monteiro, Concrete Microstructure, Properties, and Materials, third ed., McGraw-Hill, New York, 2006.